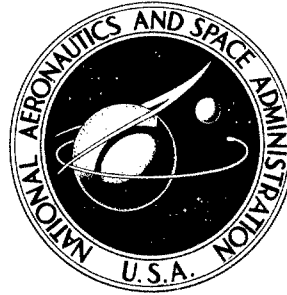


74087

F

**NASA CONTRACTOR
REPORT**



NASA CR-1288

NASA CR-1288

AMPTIAC

DISTRIBUTION STATEMENT A
Approved for Public Release
Distribution Unlimited

EXPERIMENTAL AND ANALYTICAL INVESTIGATIONS ON MULTIPLE LIQUID IMPACT EROSION

by A. Thiruvengadam and S. L. Rudy

Prepared by
HYDRONAUTICS, INC.
Laurel, Md.
for

Reproduced From
Best Available Copy

20000908 230

DMIC-74087

fat
DMIC
B

NASA CR-1288

EXPERIMENTAL AND ANALYTICAL INVESTIGATIONS
ON MULTIPLE LIQUID IMPACT EROSION

By A. Thiruvengadam and S. L. Rudy

MAR-1969

Distribution of this report is provided in the interest of information exchange. Responsibility for the contents resides in the author or organization that prepared it.

Issued by Originator as Technical Report 719-1

Prepared under Contract No. NASw-1608 by
HYDRONAUTICS, INC.
Laurel, Md.

for

NATIONAL AERONAUTICS AND SPACE ADMINISTRATION

For sale by the Clearinghouse for Federal Scientific and Technical Information
Springfield, Virginia 22151 - CFSTI price ~~\$3.00~~

FOREWORD

The work described herein was performed by HYDRONAUTICS, Incorporated, Laurel, Maryland under NASA Contract NASW-1608 with the technical management of Mr. S. V. Manson, Nuclear Systems and Space Power Division, Code RNP, NASA Headquarters, Washington, D. C.

TABLE OF CONTENTS

	Page
SUMMARY.....	1
INTRODUCTION.....	3
EXPERIMENTAL FACILITY AND TECHNIQUES.....	5
The Jet Impact Erosion Facility.....	5
Photographing the Jet Impact Phenomenon.....	5
High Frequency Fatigue Testing Technique.....	6
EXPERIMENTAL PROCEDURE.....	9
Determination of Threshold Velocities.....	9
Determination of High Frequency Endurance Limit.....	11
Determination of Rate of Erosion as a Function of Exposure Time.....	11
RESULTS AND ANALYSIS	12
Correlation of Threshold Water Hammer Stresses with High Frequency Endurance Limit.....	12
Effect of Time of Exposure to Multiple Liquid Impacts on the Rate of Erosion.....	15
Correlation with the Theory of Erosion.....	17
The Relationship Between the Impact Velocity and the Rate of Erosion.....	23
COMPARISON OF LIQUID IMPACT EROSION AND CAVITATION EROSION THROUGH SCANNING ELECTRON MICROSCOPY.....	26
CONCLUSIONS.....	28
APPENDIX A - DESIGN OF ROTATING DISK CAPABLE OF HOLDING SIX SPECIMENS.....	30
APPENDIX B - DERIVATION OF ELEMENTARY THEORY OF EROSION....	33
REFERENCES	47

LIST OF FIGURES

- Figure 1 - General View of Multiple Liquid Impact Erosion Facility
- Figure 2 - Typical Water Column and Spray Pattern During Specimen Progression
- Figure 3 - Block Diagram of the Magnetostriction Apparatus Used for High Frequency Fatigue Tests
- Figure 4 - Notched High Frequency Fatigue Specimen
- Figure 5 - Basic Approach for the Design of Dumb-Bell Shaped Fatigue Specimen
- Figure 6 - Dumb-Bell Shaped High Frequency Fatigue Specimen
- Figure 7 - Comparison of Theoretical Strain and Measured Strain for Dumb-Bell Type Fatigue Specimens
- Figure 8 - 316 Stainless Steel Specimen Run 20 Hours at 150 ft/sec for 8.3×10^6 Impacts to Threshold
- Figure 9 - Surface Roughness Profile at Threshold and at Fracture
- Figure 10 - Relationship Between Impact Speed and the Number of Impacts Till Initial Plastic Dents Are Obtained on 316 Stainless Steel and on 1100-0 Aluminum
- Figure 11 - 1100-0 Aluminum Fatigue Data at High Frequency-- Relationship Between the Stress Amplitude and the Number of Cycles to Fracture
- Figure 12 - 316 Stainless Steel Fatigue Data at High Frequency --Relationship Between the Stress Amplitude and the Number of Cycles to Fracture
- Figure 13 - Effect of Time on Cavitation Damage Rate for Various Amplitudes (Reference 9)
- Figure 14 - Effect of Time on Intensity of Erosion
- Figure 15 - Rate of Volume Loss as a Function of Time at Three Velocities for 316 Stainless Steel

- Figure 16 - Rate of Volume Loss as a Function of Time at Three Velocities for 316 Stainless Steel
- Figure 17 - Rate of Volume Loss as a Function of Time at Three Velocities for 1100-0 Aluminum
- Figure 18 - Rate of Volume Loss as a Function of Time at Three Velocites for 1100-0 Aluminum
- Figure 19 - Theoretical Prediction of the Effect of Time on Intensity of Erosion When $n=2$
- Figure 20 - Comparison of Experimental Results with the Erosion Theory for 1100-0 Aluminum
- Figure 21 - Comparison of Experimental Results with the Erosion Theory for 316 Stainless Steel
- Figure 22 - Weibull Distribution for High Frequency Fatigue of 1100-0 Aluminum at Room Temperature
- Figure 23 - Weibull Distribution for High Frequency Fatigue of 316 Stainless Steel at Room Temperature
- Figure 24 - Relationship Between Peak Rate of Volume Loss and the Impact Velocity
- Figure 25 - Relationship Between the Time at Which Peak Rate of Volume Loss Is Observed and the Impact Velocity
- Figure 26 - Relationship Between the Relative Impact Velocity and the Rate of Volume Loss
- Figure 27 - Microphotographs of the Test Materials Showing Structure
- Figure 28 - Comparison of Indentations Produced by Multiple Liquid Impact Erosion and by Cavitation Erosion-- Scanning Electron Microphotographs
- Figure 29 - Rotating Disk Capable of Holding Six Specimens
- Figure 30 - Definition Sketch
- Figure 31 - Theoretical Prediction of the Effect of Time on Intensity of Erosion When $n=3$

Figure 32 - Theoretical Prediction of the Effect of Time on Intensity of Erosion When $n=4$

Figure 33 - Theoretical Predictions of the Erosion Intensity When Gumbel Type Distributions Are Used

Figure 34 - Theoretical Predictions of the Cumulative Depth of Erosion

SUMMARY

This technical report summarizes the results of experimental and analytical investigations on multiple liquid (water) impact erosion of ^{all} 1100-0 ^{Al} Aluminum and 316 ^{SS} stainless steel, under contract No. NASW-1608. An existing rotating disk facility was modified so that six specimens might be simultaneously tested at three different velocities. High speed motion pictures as well as conventional movie films with stroboscopic illumination were taken to show the phenomenon of liquid jet impact with the test material in a qualitative manner.

Using this facility, the threshold ^{all} impact velocity at which visible erosion was observed after ten million impacts was determined. The threshold water hammer stress on the material corresponding to this threshold velocity, was correlated with the high frequency endurance limit corresponding to ten million fatigue cycles using the magnetostriction vibratory apparatus. The ratio between the fatigue endurance limit and the threshold water hammer stress is 1.7 for 1100-0 aluminum and 3.0 for 316 stainless steel.

A mathematical theory of erosion has been recently developed to predict the rate of cavitation erosion as a function of exposure time. This theory was extended to multiple liquid impact erosion. In this theory, it is important to know the value of a parameter called the shape parameter, α . In the original theory →

it was assumed that the shape parameter was the same as that obtained in fatigue probability distribution (Weibull distribution). However, the present investigations show that the Weibull shape parameter as obtained from a high frequency fatigue test corresponding to ten million life cycles is about 0.5 whereas the shape parameter required to predict the erosion rates is 3.0 for aluminum and 5.0 for 316 stainless steel. The implications of this result on the erosion theory are fully discussed. The probable reasons for the variation in the shape parameter are also pointed out. The usefulness of the erosion theory in practical applications is also brought forth.

An analysis of the results obtained indicates that the peak rate of erosion varies as the fifth power of the velocity of impact and the time at which the peak rate is observed varies as the one-fifth power of the impact velocity.

Scanning electron microphotographs of eroded specimens both by cavitation and by liquid impingement were compared. The process of material removal seems to be very similar in both the kinds of erosion further justifying the use of a common theory.

]

enf

INTRODUCTION

The problem of erosion caused by multiple liquid impacts can become a serious one in the development of future space nuclear power systems. In addition it is also important in wet steam or vapor turbines and in rain erosion of aircraft and missiles. The objectives of the present research program are the understanding of the mechanism and the quantitative evaluation of two aspects of multiple liquid impact erosion, namely: (i) the initiation of erosion and (ii) the rate of erosion. During the past several years of intensive research in the allied problem of cavitation erosion, the above two aspects were considered in depth (References 1 and 2). Some of the significant ideas generated through those efforts were extended to the understanding of multiple liquid impact erosion.

Specifically the major tasks of this research program are as follows:

1. To determine experimentally the threshold velocity of impact on two materials namely 1100-C aluminum and 316 stainless steel.
2. To determine the high frequency fatigue stresses for these two materials.
3. To relate the water hammer stresses corresponding to the threshold velocities with the high frequency endurance limit of these materials.

4. To determine the rate of erosion as a function of exposure time for these two materials.

5. To correlate the experimental rates with theoretically predicted rates.

6. To evaluate the dependence of the rate of erosion on the velocity of impact.

These tasks were accomplished by using the jet-impact erosion facility and the magnetostriction vibratory apparatus. The results of these investigations are presented in this report.

EXPERIMENTAL FACILITY AND TECHNIQUES

The Jet Impact Erosion Facility

The erosion test facility that was already available at the beginning of this program consisted of a rotating disk on which two specimen holders were fixed at two diametrically opposite locations. A one half horsepower motor (capable of rotating at 10,000 rpm at no load) drove the rotating disk up to a maximum peripheral speed of 350 feet per second, causing the specimen to impact two solid jets 1/16 inch in diameter. The erosion was caused by the impact of the test specimens on the solid jet at controlled speeds. This facility was improved further under the present program by replacing the drive motor with a $2\frac{1}{2}$ hp high speed motor capable of sustained operation at 20,000 rpm and a suitable variable transformer power supply for speed control. A new rotating disk capable of holding six test specimens at increased speeds was designed, fabricated and used in the present investigations. The maximum peripheral speed achieved was 700 fps. The number of jets was increased to six. Figure 1 shows the facility as it exists now after all the improvements. Appendix A contains the basic outline of the design of the rotating disk.

Photographing the Jet Impact Phenomenon

Two techniques were used to photograph the impact of the jet with the test specimen. The first method employed the high intensity strobe light to stop the motion so that conventional movie pictures at 24 frames per second could be taken. The

second method used a Hycam high speed motion picture camera capable of taking up to 8000 frames per second. The photographs provided qualitative understanding of the liquid impact phenomenon. In addition, they showed that jets were not broken up before impact and that the spray after impact did not hit the neighboring specimens. Typical photographs are shown in Figure 2.

High Frequency Fatigue Testing Technique

A magnetostriction oscillator (Figure 3) was used to produce alternating strains at the node of a resonating rod. The basic principle and the practical aspects of these tests are described in References 3 and 4. The fatigue specimen design used in the earlier studies had a sharp notch at the node (Figure 4). The notch sensitivity of the test materials at high frequencies is an unknown. In order to eliminate this limitation, a new dumb-bell shaped fatigue specimen was designed and used for all the fatigue tests under this program.

The basic approach for the design of the fatigue specimen is to use the theory developed by Neppiras (5). From this theory one can get the lengths of the fatigue specimen as shown by the example in Figure 5. Assuming an area ratio and l_1/λ , the value of l_2/λ may be determined from Neppiras' theory. In order to avoid the sharp corners, a circular arc fillet of radius R is used. The value of R can be calculated from simple geometrical considerations. This method of designing dumb-bell shaped fatigue specimens gave the dimensions within 10 to 15 percent

accuracy. Then the final adjustments are made by tuning experimentally. The dimensions of a properly tuned fatigue specimen are shown in Figure 6.

In all the fatigue studies, theoretical strain, given by the following formula (due to Neppiras (5)), was assumed to be the actual value:

$$\epsilon = \frac{G \cdot 2\pi\xi}{\lambda} \quad \text{--- -- -- -- -- [A]}$$

where

- ϵ - the strain amplitude at the node,
- ξ - the displacement amplitude at the anti-node,
- λ - the wavelength in the material, and
- G - Magnification Factor
 $= \frac{\text{Strain in stepped specimen}}{\text{Strain in uniform specimen (without step)}}$

The value of G can be calculated from Neppiras' theory. Generally one would measure the displacement amplitude ξ and the wavelength λ , and calculate the strain using a theoretical value of G. However, we attempted to verify these calculations by measuring the actual strains generated at the node in spite of many practical difficulties. Fixing a suitable strain gage to withstand the high frequency fatigue strains became a problem. The strain gage failed in fatigue. The adhesive did not hold properly under fatigue strain. Since the entire fatigue specimen has to be immersed in a cooling bath, the strain gages had to be potted with water resistant coating. These problems were solved after several trials by using different strain gage-adhesive systems. The

successful one was the type FAB-03N-12-S9 with EPY 500 adhesive supplied by Baldwin-Lima-Hamilton Electronics, Inc. The entire strain gage was potted with neoprene and vacuum cured making it impermeable to water.

The fatigue specimens were calibrated statically by using deadweights hanging from the specimen. In order to minimize bending, two universal joints were provided fore and aft of the fatigue specimens. Assuming that the static calibration holds good for the dynamic measurements also, the dynamic strains were measured at various displacement amplitudes. A comparison between the measured strains and the calculated strains is shown in Figure 7. This effort proved that the theoretical formula is accurate for our design.

EXPERIMENTAL PROCEDURE

As discussed previously, essentially the following three types of experiments were performed during this investigation:

1. Determination of Threshold Velocities,
2. Determination of the fatigue endurance limit, and
3. Determination of Erosion Rates.

The erosion tests were carried out in the jet impact erosion facility and the fatigue tests were conducted in the magnetostriction vibratory apparatus. The important details of the experimental procedure followed are described below.

Determination of Threshold Velocities

Six test specimens were attached at three radial locations in the rotating disk described previously. This enabled the observation of two specimens at a preselected test velocity ensuring the reproducibility and reliability of the experimental observation. The test specimens were 3/8 inch in diameter. The specimen surface was finished to 32 rms or better by hand polishing, thus eliminating the possibility of mechanical work hardening affecting the test results. Such carefully prepared test specimens were attached to the rotating disk and run at preselected speeds. Observation of the specimens to determine when denting or fracture occurred was adjusted to suit the test sequence. When tests were conducted at higher velocities, damage could be observed in a short time and hence the specimens were observed at

short intervals (every few minutes). At lower velocities, damage would not occur for many hours; consequently observations were made every half or one hour. The observation consisted of removing a test specimen and of observing the surface exposed to liquid impact with a 10 X magnifying glass under side lighting which would make the initial indentations "stand out" when illuminated at the proper angle to the surface. The time taken for the initiation of permanent plastic indentations on the surface of the test specimen through this procedure was recorded at different test velocities. The number of impacts were calculated from the number of revolutions made during that time multiplied by two for the two impacts per revolution. The relationship between the number of impacts and the velocity was plotted and the velocity corresponding to 10 million impacts was obtained from such a plot. This velocity is designated as the threshold velocity.

After the appearance of plastic dents on the specimen surface, this area of denting will continue to work harden as the test progresses resulting in the fracture of small fragments of material from the surface. In all our experiments, the criterion for threshold was the appearance of detectable indentation with the help of a 10 X magnifier under side lighting. The appearance of the surface after 10 million impacts at 150 fps on 316 stainless steel is shown in Figure 8. The surface roughness profile after 10 million impacts at threshold velocities is shown in Figure 9.

Determination of High Frequency Endurance Limit

The fatigue specimens were vibrated at 14.2 kcs at controlled amplitudes in the magnetostriction vibratory apparatus. The specimens were cooled by immersion in a constant temperature water bath. The amplitude was obtained from the voltage output of a precalibrated voice coil. The strain was calculated from the amplitude (using equation [A]) as discussed previously. The stress was obtained by multiplying the strain with the modulus of elasticity. The modulus of elasticity for the test material can also be determined with the vibrator by measuring the wavelength and the frequency which will give the speed of sound. The frequency was accurately measured with a frequency counter. The time to failure was noted and the number of cycles to failure was computed from the frequency.

Determination of Rate of Erosion as a Function of Exposure Time

The rate of weight loss was determined periodically by weighing the same specimen after exposure to impact at preselected velocities. Care was taken to adopt a uniform procedure in cleaning and drying the specimen before and after each test. The rate of volume loss was obtained by dividing the rate of weight loss by the density of the material. The mean depth of erosion was calculated by dividing the volume of erosion by the area of erosion. The eroded area was taken to be equal to the impact area of the jet. The actual eroded area can also be measured accurately with a planimeter.

RESULTS AND ANALYSIS

Correlation of Threshold Water Hammer Stresses with High Frequency Endurance Limit

Figure 10 shows the relationship between the velocity of impact and the number of impacts after which the indentations were observed both on 1100-0 aluminum and on 316 stainless steel. Several repeated observations showed that the threshold velocities corresponding to 10 million impacts were 50 fps for 1100-0 aluminum and 150 fps for 316 stainless steel.

When a cylindrical column of liquid impinges on the surface of a material, the maximum stress developed at the point of contact by the impact (generally known as "water hammer" stress) is derived by de Haller (6) as

$$\sigma_I = \frac{\rho_l C_l U_I}{1 + \frac{\rho_l C_l}{\rho_m C_m}} \quad [1]$$

where

- U_I = Impact velocity,
- ρ_l = Density of Liquid,
- ρ_m = Density of Material,
- C_l = Velocity of Sound in Liquid, and
- C_m = Velocity of Sound in the Material.

For the present investigations in which water was the test liquid and common metals are the test materials, the ratio $\rho_l C_l / \rho_m C_m$ is small compared to unity. Then the water hammer stress becomes

$$\sigma_I = \rho_l C_l U_I \quad [2]$$

If we assume that the impact stresses must exceed the fatigue endurance strength of the material in order for one to see any permanent deformation, then the ratio of these stresses at threshold must equal unity. However, an analysis (Reference 1) of some isolated experimental results of several earlier investigators showed that the ratio

$$\frac{\sigma_e}{\sigma_I} \approx 2 \quad [3]$$

One of the major aims of the present investigations is to check the above result by experimentally determining the threshold impact stress and the endurance limit for two materials.

The values of ρ_l and C_l for water, were obtained from published literature (for example Reference 7) and the values of U_I were obtained from Figure 10. Hence the impact stress $\rho_l C_l U_I$ could be calculated.

The high frequency fatigue strength of the two test materials were determined as described previously. The relationship between the stress amplitude and the number of cycles to failure

is shown in Figures 11 and 12. The endurance limit at 10 million cycles is 5000 psi and 30,000 psi for 1100-0 aluminum and 316 stainless steel respectively.

The pertinent data required for analysis is shown in Table 1. It can be seen that the ratio between the high frequency endurance limit and the impact stress is in the vicinity of two. Actually it is 1.7 for 1100-0 aluminum and 3.0 for 316 stainless steel. This variation may be attributed to several factors such as the following:

1. The detection of initiation of damage is by visual observation. This may introduce some uncertainties in the surface appearance of the individual metals studied.

2. Near threshold velocities, the effect of corrosive influences may produce surface discoloration and give rise to differences in observed threshold velocities. However, the surface roughness profiles rule out this possibility.

3. It is quite possible that some other mechanical property is responsible for producing the variation.

4. The de Haller equation to predict the water hammer pressure on the material may not be accurate enough for the present experimental conditions, since it is based on one-dimensional analysis for the impact of two solid bodies.

Effect of Time of Exposure to Multiple Liquid Impacts on The Rate of Erosion

The importance of exposure time on the rate of erosion was recognized and highlighted in a series of recent publications (8,9,10,11 and 12) based mainly on cavitation erosion research. The typical relationship between the test duration and the rate of erosion in a cavitation erosion test is shown in Figure 13. This relationship was divided into four zones, Figure 14 as follows:

1. Incubation Zone: The rate of erosion is very small during the early part of an erosion test. During this time, the material undergoes permanent changes due to the repeated erosive forces. Hence it is believed that the erosion incubates during this period.

2. Accumulation Zone: After the incubation, the material starts fracturing due to the repeated impacts. The rate of loss of material starts increasing with further exposure to erosion. Since this process is similar to cumulative fatigue fracture, it was called energy accumulation zone.

3. Attenuation Zone: Where enough material has been fractured, the eroded surface becomes rough with visible deep craters. In cavitation erosion and in liquid impact erosion, the liquid covering these craters cushions the impact pressures transmitted to the material. The decrease in erosion rate is believed to be due to this attenuation process and hence this zone is called the attenuation zone.

4. Steady State Zone: It is experimentally observed that after the attenuation zone, the rate of erosion becomes very nearly independent of the exposure time and hence it is called the steady state zone.

Although the above results on the effect of exposure time were observed only for cavitation erosion, there were some indications in the literature that these effects were also detectable in liquid impact erosion tests such as steam turbine erosion (13, 14), jet impact erosion (15) and rain erosion (16). A summary and discussion of all these results with a mathematical analysis was presented by Heymann (17).

At this juncture, it became crucial to conduct a few systematic experiments to verify whether such effects were noticeable in the case of multiple liquid impact erosion. As shown in Figures 15 through 18, these effects are indeed present. The materials used for the test were 316 stainless steel and 1100-0 aluminum. The results shown correspond to six velocities for each material. It may be noted that the incubation period is very noticeable at lower speeds whereas the peak rate of erosion is very pronounced at higher impact speeds.

It is necessary to understand and predict these non-linear time effects quantitatively in order to achieve meaningful correlations in the laboratory and to extrapolate laboratory data to field systems. With this aim in mind, a mathematical theory of erosion has been developed recently (2) and is summarized briefly in Appendix B.

Correlation with the Theory of Erosion

As shown in Appendix B, the following normalized differential equation of erosion can be derived with the two assumptions involving "accumulation" of energy and the "attenuation" of energy and with the definition of intensity of erosion:

$$\frac{d\bar{I}}{d\tau} + \bar{k} \frac{\bar{I}^{\frac{2n+1}{n}}}{\bar{\eta}^{1/n}} - \frac{\bar{I}}{\bar{\eta}} \frac{d\bar{\eta}}{d\tau} = 0 \quad [4]$$

where

$$\bar{I} = I_e / I_{\max},$$

$$I_{\max} = \text{Maximum Intensity of erosion,}$$

$$\tau = t/t_1,$$

$$I_e = \text{Intensity of erosion at any time } t,$$

$$t_1 = \text{the time corresponding to the maximum intensity of erosion,}$$

$$\bar{\eta} = \eta/\eta_1,$$

$$\eta = \text{the efficiency of erosion at any time } t,$$

$$\eta_1 = \text{the efficiency corresponding to the peak intensity of erosion,}$$

$$\bar{k} = \left. \frac{d\eta}{d\tau} \right|_{\tau=1}, \text{ and}$$

$$n = \text{the attenuation exponent.}$$

The general solution of this normalized differential equation is found to be

$$\bar{I} = \frac{\bar{\eta}}{\left[1 + \bar{k} \frac{n+1}{n} \int_1^{\tau} \bar{\eta} d\tau \right]^{n/n+1}} \quad [5]$$

In order to calculate \bar{I} as a function of τ , the value of n and the function $\eta(t)$ must be known. From the experience of underwater explosions, it is known that the shock pressure attenuates inversely as the distance travelled (18). Since the intensity varies as the square of the shock pressure, the value of n may be assumed to be 2.

In the original formulation of the elementary theory (2), the nature of the function $\eta(t)$ was assumed to be similar to the fatigue probability function. The physical basis for this assumption may be enunciated as follows: A fractured particle has absorbed energy from the impact forces over a number of cycles. After the cumulative absorption of these impact forces, the particle fractures from the specimen thereby producing a loss of material. In this sense, the efficiency of the erosion process is associated with the fracture of a particle of the material. If we consider the particle as a fatigue specimen, then the probability of failure of the particle after sometime is a statistical function. Based on this approach, it may be inferred

that the efficiency of energy absorption (the function $\eta(t)$) is associated with the probability of failure of a particle after a given time. There are several statistical distribution functions advanced in the literature to represent the probability of fatigue failure. Specifically, the Weibull distribution (19) was chosen for the analysis because of its wide applicability. Hence a Weibull type distribution function of the following form was assigned to η :

$$\eta = 1 - \exp(-\tau^\alpha) \quad [6]$$

The parameter α is called the Weibull shape parameter and it depends upon the material as well as the stress level. As can be seen, the above distribution becomes a simple exponential distribution where $\alpha = 1$ and the Rayleigh distribution when $\alpha = 2$. It corresponds to a nearly normal distribution when $\alpha = 3.57$ (20). Using different values of α in Equation [6], the solutions to Equation [5] were evaluated and shown in Figure 19 as a plot of the relative intensity against the relative exposure time with α as the third parameter.

At this juncture, the following points about the elementary theory discussed above are worthy of consideration:

1. The theory is not limited to the use of Weibull type distributions to represent the efficiency of energy absorption. In fact, it is also possible to use a direct relationship between the energy absorption capacity and the number of cycles of impacts. As of now no such quantitative relationship exists

although one may develop an empirical relationship to fit the available experimental data. For example Manson (21) has presented experimental evidence to show how work hardening or work softening of metals proceeds with number of fatigue cycles. The fact that the phenomenon of work hardening or work softening is important in the erosion process has been pointed out by many investigators including Engel (22). However, the state of the art is not adequate to develop a general mathematical relationship to fit the experimental data. Because of this reason, the Weibull type distributions were used as a first attempt.

2. In the elementary theory only the efficiency function $\eta(t)$ was assumed to be a statistical distribution. However, the drop size distribution (or bubble size distribution in the case of cavitation) and the surface roughness distribution are both statistical quantities. For this reason, it was pointed out in Reference 2 that a general theory of erosion would lead to an erosion distribution function, which would take into account all of the above parameters.

3. Again, it was assumed in the elementary theory, that the value of the shape parameter α , was exactly the same as one would obtain from a fatigue life distribution for the material. Another assumption involved is that the value of α is unique at all stress levels. However, it is known that the value of the shape parameter depends upon the stress level, the presence of notches, the environment and the material (19).

With this background, let us analyze the experimental data shown in Figures 15 through 18. These data are reduced in the non-dimensional form by dividing the rate of loss at any time by the peak rate of loss, the latter being obtained from the curve which fitted the experimental data best. The time is normalized with respect to the time at which the peak erosion rate is observed. The data points collected at five different velocities are shown in Figures 20 and 21 for 1100-0 aluminum and for 316 stainless steel respectively. The solid lines in these figures are theoretical predictions of Equation [5]. Weibull distributions of the type given by Equation [6] are used for the efficiency function assuming $\alpha = 3$ for 1100-0 aluminum and $\alpha = 5$ for 316 stainless steel. This result in itself is very useful in predicting the erosion rates. However, it also leads to the following question of scientific interest.

How does the value of the shape parameter, α as determined in the above erosion test compare with the shape parameter, α as obtained from an actual fatigue life distribution for each material? In order to make a distinction between the two shape parameters, let us call the shape parameter for the erosion distribution as α_1 , and the shape parameter for the fatigue life distribution as α_2 .

The fatigue life distribution for the two materials were experimentally determined using the high frequency fatigue technique described earlier in this report. Twenty-nine samples of 1100-0 aluminum were tested at a stress level of 5000 psi corresponding to a mean life of 10 million cycles (see Table 2).

Also shown in this table are the Weibull distribution functions. The data reduction has been carried out as suggested in Reference 2. Figure 22 shows the plot of the results in a Weibull probability paper. The Weibull shape parameter, α_2 , actually varies with the number of cycles particularly below 500,000 cycles. However, for the most part, the Weibull shape parameter, α_2 , is nearly 0.5. The mean life is 3×10^7 cycles. Similar results are shown in Table 3 and in Figure 23 for 316 stainless steel. The value of α_2 is close to 0.4 for this case. Again, the Weibull plot does not seem to be a straightline for the entire range of the life cycles. For example in the case of 316 stainless steel data, at the lower end of the life cycles, the value of α_2 is close to 1.0. The same trend is noticeable for the case of 1100-0 aluminum.

In any case, it is clear that the value of the shape parameter α_2 as obtained by high frequency fatigue tests on dumb-bell shaped fatigue specimens at a stress level corresponding to the mean life of twenty to thirty million cycles is much lower than the value of the shape parameter α_1 , as determined from the erosion curve. The following factors must be taken into consideration in understanding the above result.

1. The erosion was produced at much higher stress levels than the stress level at which fatigue distribution was determined. It is known that the value of α is much higher at higher stress levels (Reference 19).

2. The fracture in erosion is produced at sharp corners and stress concentrations whereas the dumb-bell shaped fatigue specimen is rather idealized when compared to the fractured particle.

3. As pointed out previously, the influence of other factors such as surface roughness distribution and drop size distribution must also be considered in addition to the fatigue life distribution.

While these aspects are under continued investigations, the results so far obtained do provide very useful practical results. For example, the effect of test duration may be quantitatively reduced in a generalized form. It can be mathematically expressed if the shape parameter α_1 is determined through an erosion test for each material. As shown in Appendix B this relationship can be integrated so that the cumulative depth of erosion may be predicted at different intensities of erosion.

The Relationship Between the Impact Velocity and the Rate of Erosion

The relationship between the velocity of impact and the rate of erosion is very important in understanding the phenomenon of erosion as well as in extrapolating laboratory data to practical problems. Heymann (23) has summarized most of the available information on this aspect. Without considering the effect of test duration, several investigators have found that the rate of erosion varies as some power of the impact velocity as listed below (23).

<u>Author</u>	<u>Exponent</u>
Honegger	2.0
Pearson	2.6
Hoff et.al.	5 - 7
Hobbs	5

After analyzing all these data, Heymann (23) came to the conclusion that the exponent will generally be of the order of 5. Heymann also pointed out that the exponent is close 2.5 if the threshold velocity is subtracted from the actual impact velocity.

In order to see how far these conclusions agree with our experimental results, the peak rate of volume loss as shown in Figures 15 through 18 are plotted as a function of impact velocity in Figure 24. (See also Table 4). The solid lines in Figure 24 correspond to a fifth power variation. In other words, the peak rate of erosion does vary as the fifth power of the velocity of impact. Similarly the time at which the peak rate is observed is also shown plotted against impact velocity in Figure 25 and the solid lines in this figure correspond to a one fifth power variation. To summarize these results,

$$I_{\text{peak}} \propto U^5 \quad [7]$$

$$t_1 \propto U^{1/5} \quad [8]$$

where

I_{peak} is the maximum intensity of erosion,
 t_1 is the time at which the peak intensity is
observed, and
 U is the impact velocity.

In Figure 26, the peak rate of erosion is plotted against the difference between the actual impact velocity and the threshold velocity for the test material. Here again the solid lines correspond to an exponent of five and may be expressed empirically as

$$I_{\text{peak}} \propto (U - U_T)^5 \quad [9]$$

where U_T is the threshold velocity for the material. This result does not agree with the conclusion reached by Heymann (23).

COMPARISON OF LIQUID IMPACT EROSION
AND CAVITATION EROSION THROUGH
SCANNING ELECTRON MICROSCOPY

An attempt has been made in this report to make use of the theory of erosion developed on the basis of ideas, concepts and experience accumulated through intensive research on cavitation erosion. Hence it is essential to consider how far the material removal process in multiple liquid impact erosion is similar to the material removal in cavitation erosion. The main objective of this approach is to establish a common quantitative framework for both the kinds of erosion.

In order to compare the indentations and fracture produced by the two different erosion processes, carefully prepared and metallurgically polished specimens (see the photomicrographs in Figure 27) were subjected to both types of erosion separately. Cavitation erosion was produced in a magnetostriction type vibratory apparatus whereas the multiple liquid impact erosion was produced in the facility described in this report. Scanning electron micrographs were taken with the kind assistance of Mr. Robert Anstead of Goddard Space Flight Center and reproduced in Figure 28. Since the eroded surface is very rough, scanning electron micrography offers the most suitable depth of focus which cannot be obtained either by light microscopy or by conventional electron microscopy. (Scanning electron microscopy is a relatively new technique in which the electrons liberated from the specimen are scanned in synchronism with the electron-probe scanning the specimen (24)).

As seen in Figure 28, the similarity of the mechanism of material removal is great. The plastic indentations overlapping each other and producing raised craters are clearly seen in both cases. Such overlapping indentations cause the fracture of particles of the test material. These observations further justify the use of the erosion theory developed for cavitation erosion to liquid impact erosion.

CONCLUSIONS

The following conclusions may be reached from the experimental and analytical investigations on the multiple liquid impact erosion phenomenon so far carried out:

1. The ratio between the high frequency endurance limit and the impact stress is in the vicinity of two. Actually it is 1.7 for 1100-0 aluminum and 3.0 for 316 stainless steel.

2. The rate of erosion caused by multiple liquid impacts is very much dependent on the exposure time. The rate of erosion is small in the beginning (incubation zone), increases (accumulation zone), then decreases (attenuation zone) and reaches a relatively steady rate (steady state zone). This behavior is very close to the observations made on cavitation erosion.

3. The theory of erosion developed to predict cavitation erosion rates, was used to correlate with the rate of erosion produced by multiple liquid impact erosion. The shape parameter as obtained in a high frequency fatigue curve at stress levels corresponding to ten million cycles is much lower than the shape parameter required to predict the erosion rates. However, if a proper shape parameter is assumed by inspection of the normalized erosion data, then the correlation between the theory and experiments is good. The implications of these findings and the further modifications to the theory as a result of these findings are fully discussed in the report.

4. The peak rate of erosion varies as the fifth power of the velocity of impact. The time at which the peak rate of erosion is observed varies as the one-fifth power of the impact velocity.

5. Scanning-electron-microphotographs of erosion caused both by cavitation and by multiple liquid impacts show close similarity of the process of material removal by both kinds of erosion.

APPENDIX A

DESIGN OF ROTATING DISK CAPABLE OF HOLDING SIX SPECIMENS

Figure 29 shows a sketch of the rotating disk capable of holding six specimens. The specimens are located at three radii thereby yielding test results at three velocities for every run. Since there are two specimens at each radius, the reproducibility of data is verified at each run.

Power Requirements: Since the rotating disk contains both a circular disk and two whirling arms extending from the disk, the power required to rotate the disk was calculated in two separate steps.

1. Power consumed by the disk is given by

$$P_D = C_m \frac{\rho_a}{2} \omega^3 R_D^5 \quad [A1]$$

where

- C_m is the moment coefficients given in Reference 25,
 ρ_a is the density of air,
 ω is the angular velocity of disk, and
 R_D is the radius of disk.

2. Power Consumed by the Whirling Arms is given by

$$P_a = C_D \rho_a \omega^3 C \left[\frac{R_o^4}{4} - \frac{R_i^4}{4} \right] \quad [A2]$$

where

C_D is the drag coefficient of the aerofoil,

C is the chord length of the aerofoil,

R_o is the outer radius of the arm, and

R_i is the inner radius of the arm.

3. Power consumed by the specimens is given by

$$P_S = C_{DS} \frac{\rho_a}{2} A \cdot U^3 \quad [A3]$$

where

C_{DS} is the drag coefficient for specimen,

A is the projected area of the specimen, and

U is the peripheral velocity of the specimen.

Stress Calculations: The area of cross-section of a whirling arm in which the stresses developed due to centrifugal forces are constant from root to tip is given by Reference 26 as follows:

$$\frac{a_r}{a_t} = \exp \left(\frac{W\omega^2 r^2}{2g\sigma} \right) \quad [A4]$$

where

a_r is the root area,

a_t is the tip area,

W is the weight per unit volume of the material,

σ is the allowable stress, and

g is the acceleration due to gravity.

Similarly the following equation gives the variation of thickness along the radius for a rotating disk of constant stress (Reference 26)

$$\frac{t_o}{t} = \exp \left(\frac{W\omega^2 r^2}{2g\sigma} \right) \quad [A5]$$

where

t_o is the thickness at the tip, and
 t is the thickness at any radius, r .

In addition to these stresses, the centrifugal stresses caused by the weight of the specimen should also be included. Calculations using the above relationships proved that the configuration shown in Figure 29 could be successfully built with 7075 aluminum alloy and operated up to 750 fps with a 2-1/2 hp motor. Subsequent operational experience shows that the above design is sound.

APPENDIX B

DERIVATION OF ELEMENTARY THEORY OF EROSION

Definition of the Intensity of Erosion

The intensity of erosion is defined as the power absorbed by unit eroded area of the material (1,2 and 8) and is given by

$$I_e = \frac{rS_e}{t} \quad [B1]$$

where

r/t is the rate of depth of erosion, and
 S_e is the erosion strength.

If the rate of depth of erosion is expressed in differential form then

$$I_e = S_e \frac{dr}{dt} \quad [B2]$$

where r is the mean depth of erosion as measured from the original surface of the material (Figure 30).

Basic Assumptions

The two basic assumptions of the theory are as follows:

1. The attenuation of the intensity of collapse or collision is assumed to be inversely proportional to the n th power of the radial distance. This may be mathematically stated as

$$I_i = \frac{A^n I_c}{(r+r_c)^n} \quad [B3]$$

where

- I_i is the intensity of impact,
- I_c is intensity of collapse or collision,
- r is the radial distance (Figure 30),
- A is a proportionality constant with length as dimension, and
- n is the attenuation exponent.

2. The second assumption is that the intensity of erosion is related to the intensity of impact in the following manner

$$I_e = \eta I_i \quad [B4]$$

where η is a material property governing the efficiency of energy absorption. It is also further assumed that the efficiency of absorption, η is time dependent

$$\eta = \eta(t)$$

Derivation of the Differential Equation of Erosion

Differentiating Equation [B4] we get

$$\frac{dI_e}{dt} = \frac{d\eta}{dt} I_i + \eta \frac{dI_i}{dt} \quad [B5]$$

Differentiating Equation [B3], we get

$$\frac{dI_i}{dt} = A^n I_c \frac{(-n)}{(r+r_c)^{n+1}} \frac{dr}{dt} \quad [B6]$$

Furthermore from Equation [B3]

$$(r+r_c)^n = \frac{A^n I_c}{I_i} ;$$

$$(r+r_c)^{n+1} = \left(\frac{A^n I_c}{I_i} \right)^{n+1/n} \quad [B7]$$

From Equation [B2]

$$\frac{dr}{dt} = \frac{I_e}{S_e} \quad [B8]$$

Hence Equation [B6] becomes

$$\begin{aligned} \frac{dI_i}{dt} &= (-n) \frac{A^n I_c}{\left(\frac{A^n I_c}{I_i} \right)^{(n+1)/n}} \cdot \frac{I_e}{S_e} \\ &= \frac{-n A^n I_c}{\left(A^n I_c \right)^{n+1/n}} \cdot \left(\frac{I_e}{I_i} \right)^{(n+1)/n} \cdot \frac{I_e}{S_e} \quad [B9] \end{aligned}$$

since $I_i = \frac{I_e}{\eta}$ from Equation [B4]. Substituting Equation [B9] in Equation [B5]

$$\begin{aligned} \frac{dI_e}{dt} &= \frac{I_e}{\eta} \frac{d\eta}{dt} + \eta \frac{(-n) A^n I_c}{\left(A^n I_c\right)^{n+1/n}} \left(\frac{I_e}{\eta}\right)^{(n+1)/n} \frac{I_e}{S_e} \\ &= \frac{I_e}{\eta} \frac{d\eta}{dt} - \frac{k I_e^{(2n+1)/n}}{\eta^{1/n}} \end{aligned}$$

where

$$k = \frac{n}{\left(A^n I_c\right)^{1/n} S_e}$$

Hence the differential equation of erosion is given by

$$\frac{dI_e}{dt} + \frac{k I_e^{(2n+1)/n}}{\eta^{1/n}} - \frac{I_e}{\eta} \frac{d\eta}{dt} = 0 \quad [B10]$$

Normalized Differential Equation

The Equation [B10] can be normalized with respect to the parameters corresponding to the maximum intensity of damage observed in experiments. At

$$t = t_1$$

$$I_e = I_{\max}$$

$$\frac{dI_e}{dt} = 0$$

$$\eta = \eta_1$$

Then

$$\tau = \frac{t}{t_1} \quad ; \quad d\tau = \frac{dt}{t_1}$$

$$\bar{I} = \frac{I_e}{I_{\max}} \quad ; \quad d\bar{I} = \frac{dI_e}{I_{\max}}$$

$$\bar{\eta} = \frac{\eta}{\eta_1} \quad ; \quad d\bar{\eta} = \frac{d\eta}{\eta_1}$$

Since

$$\frac{dI_e}{dt} = 0 \text{ at } t = t_1$$

Equation [B10] becomes

$$\frac{k I_{\max}^{\frac{2n+1}{n}}}{\eta_1^{1/n}} = \frac{I_{\max}}{\eta_1} \left. \frac{d\eta}{dt} \right|_{t=t_1}$$

$$k = \frac{I_{\max}^{-(n+1)/n}}{\eta_1^{n-1/n}} \left. \frac{d\eta}{dt} \right|_{t_1} \quad [B11]$$

Now Equation [10] may be written as

$$\frac{I_{\max}}{t_1} \frac{d\bar{I}}{d\tau} + \frac{k I_{\max}^{\frac{2n+1}{n}}}{\eta_1^{1/n}} \frac{\bar{I}^{\frac{2n+1}{n}}}{\bar{\eta}^{1/n}} - \frac{I_{\max}}{\eta_1} \frac{\bar{I}}{\bar{\eta}} \frac{\eta_1}{t_1} \frac{d\bar{\eta}}{d\tau} = 0$$

Hence,

$$\frac{d\bar{I}}{d\tau} + \frac{\bar{k} \bar{I}^{\frac{2n+1}{n}}}{\bar{\eta}^{1/n}} - \frac{\bar{I}}{\bar{\eta}} \frac{d\bar{\eta}}{d\tau} = 0 \quad [B12]$$

where

$$\bar{k} = \frac{k I_{\max}^{\frac{n+1}{n}} t_1}{\eta_1^{1/n}}$$

(from Equation [B11])

$$\begin{aligned} & \frac{-(n+1)/n}{\eta_1^{n-1/n}} \frac{I_{\max}^{\frac{n+1}{n}} t_1}{\eta_1^{1/n}} \frac{d\eta}{dt} \Big|_{t_1} \\ &= \frac{t_1}{\eta_1} \frac{d\eta}{dt} \Big|_{t_1} \end{aligned}$$

Hence,

$$\bar{k} = \frac{d\bar{\eta}}{d\tau} \Big|_{\tau=1} \quad [B13]$$

General Solution of the Normalized Differential Equation

Let

$$z = \bar{I}^{-\left(\frac{n+1}{n}\right)}$$

$$dz = -\left(\frac{n+1}{n}\right) \bar{I}^{-\frac{2n-1}{n}} d\bar{I}$$

Equation [B12] becomes

$$-\frac{n}{n+1} \bar{I}^{-\frac{2n+1}{n}} \frac{dz}{d\tau} + \frac{\bar{k} \bar{I}^{-\frac{2n+1}{n}}}{\bar{\eta}^{1/n}} - \frac{\bar{I}}{\bar{\eta}} \frac{d\bar{\eta}}{d\tau} = 0$$

$$\frac{dz}{d\tau} + \frac{n+1}{n} \frac{1}{\bar{\eta}} \frac{d\bar{\eta}}{d\tau} z = \frac{n+1}{n} \frac{\bar{k}}{\bar{\eta}^{1/n}}$$

This is of the form

$$\frac{dz}{d\tau} + f_1(\bar{\eta}) z = f_2(\bar{\eta})$$

General solution of this equation is

$$z = \exp[-\int f_1(\bar{\eta})d\tau] \int [\exp \int f_1(\bar{\eta})d\tau] f_2(\bar{\eta})d\tau$$

$$+ C \exp[-\int f_1(\bar{\eta})d\tau] = \exp[-\int f_1(\bar{\eta})d\tau][F(\bar{\eta}) + C]$$

$$\int f_1(\bar{\eta})d\tau = \int \frac{n+1}{n} \frac{1}{\bar{\eta}} \frac{d\bar{\eta}}{d\tau} d\tau$$

$$= \frac{n+1}{n} \ln \bar{\eta}$$

$$= \ln(\bar{\eta})^{n+1/n}$$

$$\exp[-\int f_1(\bar{\eta})d\tau] = \exp[-\ln(\bar{\eta})^{-(n+1)/n}]$$

$$= (\bar{\eta})^{-n+1/n}$$

$$\exp[\int f_1(\bar{\eta})d\tau] = (\bar{\eta})^{(n+1)/n}$$

$$F(\bar{\eta}) = \int \bar{\eta}^{n+1/n} \cdot \frac{n+1}{n} \frac{\bar{k}}{\bar{\eta}^{1/n}} d\tau = \bar{k} \frac{n+1}{n} \int \bar{\eta} d\tau$$

Hence the general solution becomes

$$z = (\bar{\eta})^{-n+1/n} \left[\bar{k} \frac{n+1}{n} \int \bar{\eta} d\tau + C \right]$$

$$\bar{I} = \frac{\bar{\eta}}{\left[C + \frac{n+1}{n} \bar{k} \int \bar{\eta} d\tau \right]^{n/n+1}} \quad [B14]$$

Boundary conditions

$$\text{At } \tau = 1 ; \bar{I} = 1 ; \bar{\eta} = 1.$$

Hence

$$C + \frac{n+1}{n} \bar{k} \int_0^1 \bar{\eta} d\tau = 1$$

$$C = 1 - \frac{n+1}{n} \bar{k} \int_0^1 \bar{\eta} d\tau$$

Hence [B14] becomes

$$\bar{I} = \frac{\bar{\eta}}{\left[1 + \left(\frac{n+1}{n} \right) \bar{k} \left\{ \int_0^{\tau} \bar{\eta} d\tau - \int_0^1 \bar{\eta} d\tau \right\} \right]^{n/n+1}}$$

$$\bar{I} = \frac{\bar{\eta}}{\left[1 + \frac{n+1}{n} \bar{k} \int_1^{\tau} \bar{\eta} d\tau \right]^{n/n+1}} \quad [\text{B15}]$$

If $n = 2$

$$\bar{I} = \frac{\bar{\eta}}{\left[1 + \frac{3}{2} \bar{k} \int_1^{\tau} \bar{\eta} d\tau \right]^{2/3}}$$

When Weibull type distributions are used,

$$\eta = 1 - \exp(-\tau^\alpha) \quad [B16]$$

At $\tau = 1$ $\eta_1 = 1 - \frac{1}{e} = \frac{e-1}{e}$

$$\bar{\eta} = \frac{e}{e-1} [1 - \exp(-\tau^\alpha)]$$

$$\frac{d\bar{\eta}}{d\tau} = \frac{e-1}{e} [\alpha \tau^{\alpha-1} \exp(-\tau^\alpha)]$$

At $\tau = 1$

$$\left. \frac{d\bar{\eta}}{d\tau} \right|_{\tau=1} = \frac{e}{e-1} \cdot \frac{\alpha}{e}$$

Hence

$$\bar{k} = \frac{\alpha}{e-1}$$

$$\bar{I} = \frac{\frac{e}{e-1} [1 - \exp(-\tau^\alpha)]}{\left[1 + \frac{1.5\alpha}{e-1} \int_1^{\tau} \frac{e}{e-1} [1 - \exp(-\tau^\alpha)] d\tau \right]^{2/3}} \quad [B17]$$

From Equation [B17], \bar{I} is calculated as a function of τ for various values of α as shown in Figure 19. Figures 31 and 32 show the same relationships when $n = 3$ and 4 respectively. When Gumbel type distributions are used

$$\eta = \exp[-\beta \exp(-\tau)]$$

$$\eta_1 = \exp[-\frac{\beta}{e}]$$

$$\bar{\eta} = \frac{\exp[-\beta \exp(-\tau)]}{\exp[-\beta/e]}$$

$$\bar{k} = \left. \frac{d\bar{\eta}}{d\tau} \right|_{\tau=1} = \frac{1}{\exp[-\beta/e]} \frac{\beta}{e} [\exp(-\beta/e)]$$

$$\bar{k} = \beta/e$$

Hence

$$\bar{I} = \frac{\bar{\eta}}{\left[1 + \frac{3}{2} \frac{\beta}{e} \int_1^{\tau} \bar{\eta} d\tau \right]^{2/3}} \quad [B18]$$

Figure 33 shows the variation of \bar{I} with τ for three values of β .

Cumulative Depth of Erosion

$$\bar{I} = \frac{I_e}{I_{\max}} = \frac{S_e}{I_{\max}} \cdot \frac{dr}{dt} ; I_{\max} = S_e \cdot \left(\frac{dr}{dt} \right)_{\max}$$

Boundary conditions,

$$\text{at } t = t_1, r = r_1; \bar{r} = r/r_1; \tau = t/t_1.$$

Then

$$\bar{I} = \frac{S_e r_1}{I_{\max} t_1} \frac{d\bar{r}}{d\tau}$$

Hence

$$\int \frac{S_e r_1}{t_1 I_{\max}} d\bar{r} = \int \bar{I} d\tau + C$$

$$\frac{S_e r_1}{t_1 I_{\max}} \bar{r} = \int_0^{\tau} \bar{I} d\tau + C \quad [B19]$$

Boundary conditions,

$$t = 0 ; r = 0 ; \tau = 0 ; \bar{I} = 0 ; \bar{r} = 0.$$

Hence

$$C = 0.$$

Again at

$$t = t_1, \tau = 1, \bar{r} = 1$$

$$\frac{S_e r_1}{t_1 \bar{I}_{\max}} = \int_0^1 \bar{I} d\tau$$

Equation [B19] becomes

$$\bar{r} = \frac{\int_0^{\tau} \bar{I} d\tau}{\int_0^1 \bar{I} d\tau} \quad [\text{B20}]$$

The variation of \bar{r} with τ for various values of α when $n = 2$ is shown in Figure 34.

Relationship Between the Maximum Intensity of Erosion and The Intensity of Collapse

From Equation [B11]

$$\frac{n}{\left(A \cdot I_c\right)^{1/n} S_e} = \frac{I_{\max}^{-(n+1)/n}}{\eta_1^{n-1/n}} \left. \frac{\eta_1}{t_1} \frac{d\bar{\eta}}{d\tau} \right|_{\tau=1}$$

Using Weibull type distributions and the value $n = 2$

$$\frac{2}{(A^2 I_c)^{\frac{1}{2}} S_e} = \frac{I_{\max}^{-3/2} \left(\frac{e-1}{e}\right)^{\frac{1}{2}} \alpha}{t_1 (e-1)}$$

$$I_{\max}^{3/2} = \frac{\alpha}{2[e(e-1)]^{\frac{1}{2}}} \frac{I_c^{\frac{1}{2}} S_e A}{t_1} \quad [B21]$$

Relationship Between Erosion Strength and Maximum Rate of Erosion

From Equation [B21]

$$(\dot{r}_{\max})^{3/2} S_e^{3/2} = M I_c^{1/2} \frac{A S_e}{t_1}$$

where

$$M = \frac{\alpha}{[e(e-1)]^{\frac{1}{2}}}$$

$$\dot{r}_{\max} = \left. \frac{dr}{dt} \right|_{\max} \quad \text{at } t = t_1$$

Hence

$$S_e = \frac{A^2 I_c M^2}{t_1^2 (\dot{r}_{\max})^3} \quad [B22]$$

REFERENCES - 74087

1. Thiruvengadam, A., "The Concept of Erosion Strength," HYDRONAUTICS, Incorporated Technical Report 233-9, December 1965. (See Proc. Symp. on Erosion by Cavitation or Impingement, ASTM Annual Meeting 1966, ASTM Special Publication No. 408, Philadelphia, 1967).
2. Thiruvengadam, A., "Theory of Erosion," HYDRONAUTICS, Incorporated Technical Report 233-11, March 1967. (See also Proc. Second Meersburg Conference on Rain Erosion, August 1967. Published by Royal Aircraft Establishment, Farnborough, England).
3. Thiruvengadam, A., "High Frequency Fatigue of Metals and Their Cavitation Damage Resistance," Technical Report 233-6, HYDRONAUTICS, Incorporated, December, 1964. (See also Paper 65-WA-UnT-4, Journal of Engineering for Industry, Transactions, Am. Soc. Mechanical Engrs. Vol. 88, Series B, No. 3, August 1966). ✓
4. Thiruvengadam, A., and Preiser, H. S., "Cavitation Damage in Liquid Metals," HYDRONAUTICS, Incorporated Technical Report 467-Final, NASA CR-72035, November 1965.
5. Neppiras, E. A., "Techniques and Equipment for Fatigue Testing at Very High Frequencies," Proc. ASTM, Vol. 59, 1959, pp. 691-709.
6. Bowden, F. P., and Brunton, J. H., "The Deformation of Solids by Liquid Impact at Supersonic Speeds," Proc. Royal Society, London, A., Vol. 263, October 1961, pp. 433-450.
7. Greenspan, M. and Tschiegg, C. E., "Speed of Sound in Water by a Direct Method," Jour. Research of the National Bureau of Standards, Vol. 59, No. 4, October 1957.

8. Thiruvengadam, A., "A Comparative Evaluation of Cavitation Damage Test Devices," HYDRONAUTICS, Incorporated Technical Report 233-2, November 1963 (See also Proc. Symp. on Cavitation Research Facilities and Techniques, ASME Publication, New York, May 1964).
9. Thiruvengadam, A. and Preiser, H. S., "On Testing Materials for Cavitation Damage Resistance," HYDRONAUTICS, Incorporated Technical Report 233-3, October 1963. (See also Jour. Ship Research, Vol. 8, No. 3, December 1964).
10. Eisenberg, P., Preiser, H. S., and Thiruvengadam, A., "On the Mechanisms of Cavitation Damage and Methods of Protection," Trans. SNAME, Vol. 73, 1965.
11. Plesset, M. S., and Devine, R. E., "Effect of Exposure Time on Cavitation Damage," Trans. ASME, Jour. Basic Engr., December, 1966.
12. Hobbs, J. M., "Experience with a 20 kc/s Cavitation Erosion Test," Symp. on Erosion by Cavitation or Impingement, ASTM Annual Meeting, Atlantic City, June 1966.
13. Smith, A., Kent, R. P., and Armstrong, R. L., "Erosion of Steam Turbine Blade Shield Materials," Symp. on Erosion by Cavitation or Impingement, ASTM Annual Meeting, Atlantic City, June 1966 (See also Proc. Discussion on Deformation of Solids by the Impact of Liquids, Phil. Trans. Royal Society of London, Vol. 260, July 1966, p. 209).
14. Baker, D.W.C., Jolliffe, K. H., and Pearson, D., "The Resistance of Materials to Impact Erosion Damage," Ibid, p.193.
15. Marriott, J. B., and Rowden, G., "The Erosion of a Cobalt-Chromium Alloy by Liquid Impact," Ibid p. 144.
16. Busch, H., Hoff, G. and Langbein, G., "Rain Erosion Properties of Materials," Ibid p. 168 (See also Proc. Symp. Erosion by Cavitation or Impingement, ASTM Special Publication 408, Philadelphia, 1967).

17. Heymann, F. J., "On the Time Dependence of the Rate of Erosion Due to Liquid Impact or Cavitation," Proc. Symp. Erosion by Cavitation or Impingement, ASTM Special Publication 408, Philadelphia, 1967.
18. Cole, R. H., "Under Water Explosions," Princeton University Press, Princeton, New Jersey, 1948.
19. Weibull, W., "Fatigue Testing and Analysis of Results," Pergamon Press, New York, 1961.
20. A Guide for Fatigue Testing and the Statistical Analysis of Fatigue Data (Supplement to Manual on Fatigue Testing, STP No. 91) ASTM Special Technical Publication No. 91-A (Second Edition, Philadelphia, 1963).
21. Manson, S. S., "Fatigue-A Complex Subject - Some Simple Approximations," The William M. Murray Lecture, Experimental Mechanics, Vol. 5, No. 7, July 1965, pp. 193-226.
22. Engel, O. G., Written discussion of Heymann's paper, Reference 17 of this report, 1966. See also Proc. Turbine Erosion Conference, Jet Propulsion Laboratory, 1967.
23. Heymann, F. J., "A Survey of Clues to the Relationship Between Erosion Rate and Impingement Conditions," Preprint Volume of papers presented at the 2nd Conference on Rain Erosion held in Meersburg, West Germany, August 1967. Distributed by the Organizers, Dornier-System GmbH, Friedrichshafen /Bodensee, Germany.
24. Oatley, C. W., The Scanning Electron Microscope, New Scientist, 1958, 5, 153.
25. Schlichting, H., "Boundary Layer Theory," Fourth Edition McGraw Hill Book Company, Inc., New York, 1962.
26. Vincent, E. T., "The Theory and Design of Gas Turbines and Jet Engines," First Edition, McGraw Hill Book Company, Inc., New York, page 487, 1950.

TABLE 1

Material	Experimentally Determined Fatigue Strength at 10^7 Cycles $= \sigma_e$; psi	Material Density ρ_m ; slugs/ft ³	Sound Speed in Material $= C_m$; ft/sec	Threshold Velocity U_I^* ft/sec	Water Hammer Pressure P_I ; psi	$\frac{\sigma_e}{P_I}$
1100-0 Aluminum	5000	5.25	16,500	50	3000	1.7
316 Stainless Steel	30,000	15.45	16,300	150	9700	3.0

NOTE*

These Velocities Correspond to 10^7 Liquid Impacts after which some permanent sign of erosion was noticed.

TABLE 2

Test Results and Weibull Distribution
Function for Fatigue Failures

Material:	1100-0 Al.	Frequency:	14.2 kcs
Sample Size:	n = 29 specimens	Stress Level:	5000 psi
Temperature:	Room temperature water bath		
Order q	No. of Cycles to Failure, N	Mean Rank $100 \left(\frac{q}{n+1} \right) = F(N) \times 100$	
1	2.14×10^5	3.33	
2	2.29×10^5	6.66	
3	4.00×10^5	9.99	
4	4.27×10^5	13.33	
5	5.30×10^5	16.66	
6	5.40×10^5	19.99	
7	9.25×10^5	23.32	
8	1.17×10^6	26.65	
9	1.93×10^6	29.99	
10	4.49×10^6	33.33	
11	6.00×10^6	36.66	
12	8.64×10^6	39.99	
13	1.09×10^7	43.33	
14	1.92×10^7	46.66	
15	1.98×10^7	49.99	
16	2.32×10^7	53.33	
17	2.56×10^7	56.66	
18	2.56×10^7	59.99	

TABLE 2 (Continued)

Order q	No of Cycles to Failure, N	Mean Rank $100 \left(\frac{q}{n+1} \right) = F(N) \times 100$
19	2.73×10^7	63.33
20	3.58×10^7	66.66
21	3.84×10^7	69.99
22	3.95×10^7	73.33
23	4.72×10^7	76.66
24	5.55×10^7	79.99
25	8.17×10^7	83.33
26	8.99×10^7	86.66
27	1.075×10^8	89.99
28	1.20×10^8	93.33
29	1.66×10^8	96.66

TABLE 3

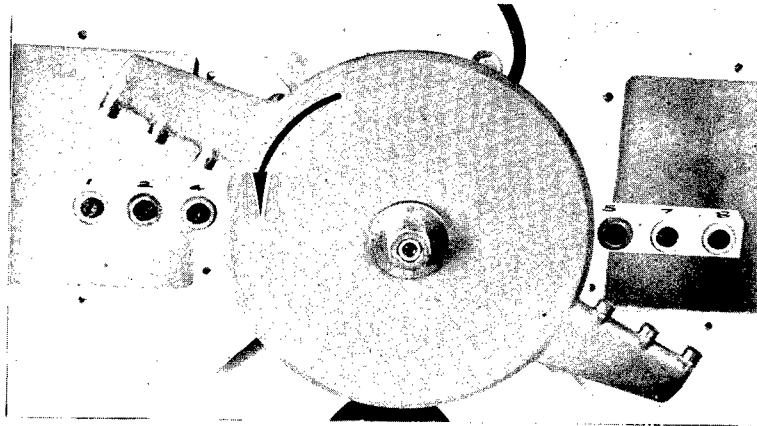
Test Results and Weibull Distribution Function
For Fatigue Failures

Material:	316 S. S.	Frequency:	14.2 kcs
Sample Size:	n = 20 specimens	Stress Level:	30,000 psi
Temperature:	Room temperature Water Bath		
Order q	No. of Cycles to Failure, N	Mean Rank $100 \frac{q}{n+1} = F(N) \times 100$	
1	1.04×10^6	4.75	
2	1.56×10^6	9.50	
3	1.85×10^6	14.3	
4	2.56×10^6	19.0	
5	3.37×10^6	23.8	
6	4.70×10^6	28.6	
7	4.81×10^6	33.3	
8	5.53×10^6	38.1	
9	6.16×10^6	43.0	
10	1.37×10^7	47.5	
11	1.39×10^7	52.5	
12	1.60×10^7	57.0	
13	5.97×10^7	62.0	
14	6.40×10^7	66.6	
15	1.02×10^8	71.5	
16	1.37×10^8	76.0	
17	3.2×10^8	81.0	
18	4.6×10^8	86.0	
19	6.0×10^8	90.5	
20	7.96×10^8	95.0	

TABLE 4

Experimental Data Showing the Effect of Impact
Velocity on the Rate of Volume Loss

316 Stainless Steel: $U_T = 150$ fps				
No.	Velocity fps	Peak Rate cc/hr	t_1 min.	Rel. Vel. ($U-U_T$) fps $_T$
1	520	20×10^{-3}	20	370
2	436	7×10^{-3}	55	286
3	350	19×10^{-4}	120	200
4	292	8×10^{-4}	300	142
1100-0 Aluminum: $U_T = 50$ fps				
1	200	20×10^{-4}	25	150
2	166	11×10^{-4}	35	116
3	182	8×10^{-3}	12	132
4	224	20×10^{-3}	3	174
5	274	31×10^{-3}	2	224



ROTATING DISC

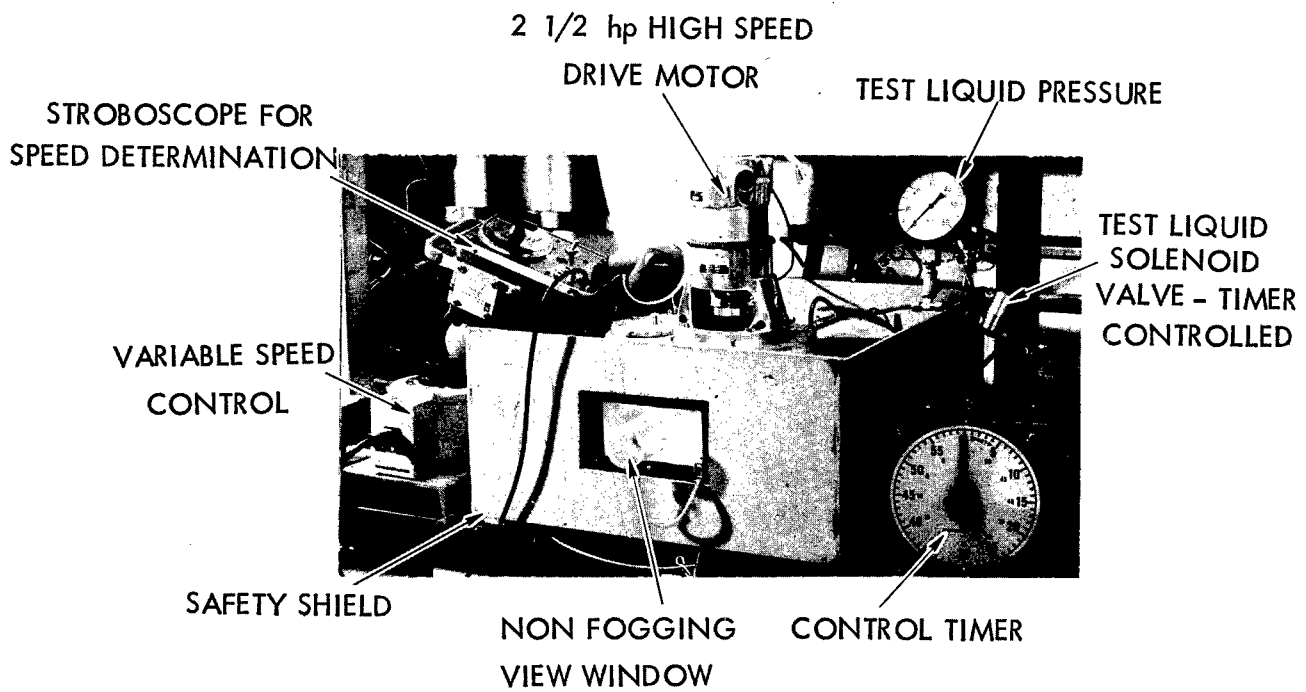
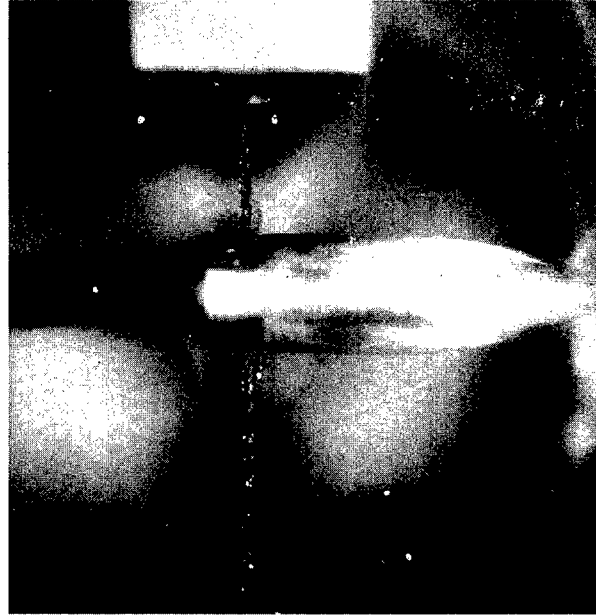
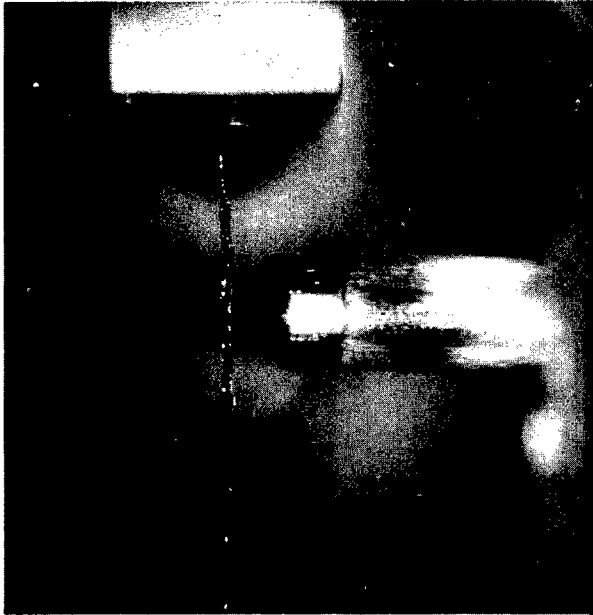


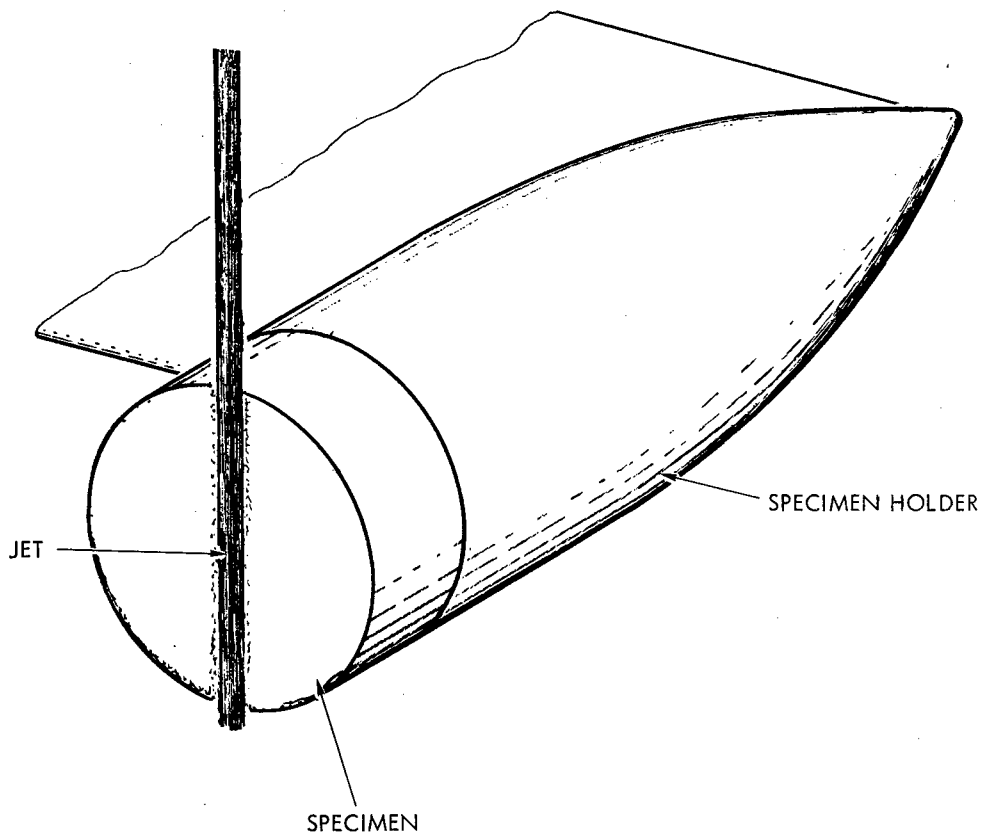
FIGURE 1- GENERAL VIEW OF MULTIPLE LIQUID IMPACT EROSION FACILITY



◁ SPECIMEN MOVING



FIGURE 2 - TYPICAL WATER COLUMN AND SPRAY PAT TERN DURING SPECIMEN PROGRESSION



IMPACT OF LIQUID JET BY TEST SPECIMEN

FIGURE 2 - CONCLUDED

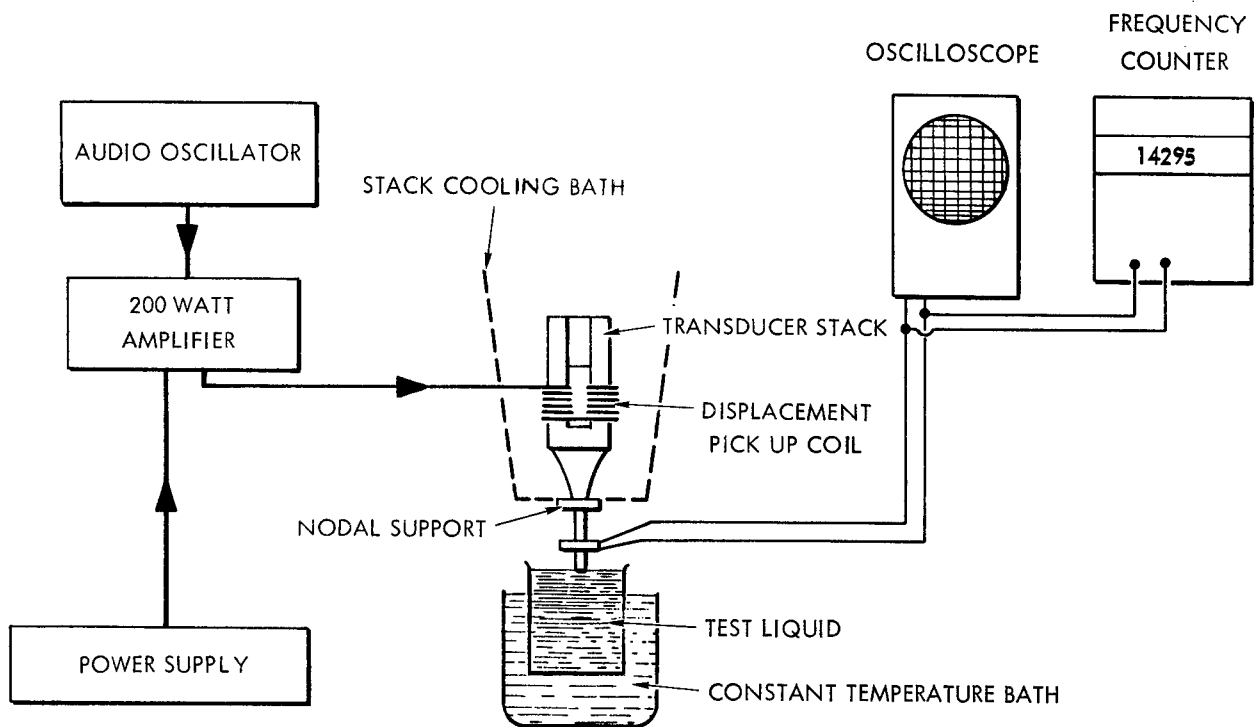


FIGURE 3 - BLOCK DIAGRAM OF THE MAGNETOSTRICTION APPARATUS USED FOR HIGH FREQUENCY FATIGUE TESTS

NOTE:

1. GROOVE (DETAIL "A") IS TO BE SMOOTH, FREE FROM CHATTER TOOL MARKS, GROOVES OR OTHER DISCONTINUITIES. THE DIMENSIONS OF THE GROOVE MUST BE IDENTICAL FOR ALL SPECIMENS IN A LOT ± 0.001 AS MEASURED WITH AN OPTICAL COMPARATOR.
2. FINISH IN GROOVE $\sqrt{63}$ OR BETTER.
3. DIMENSION "A" = HALF WAVE LENGTH OF SOUND.

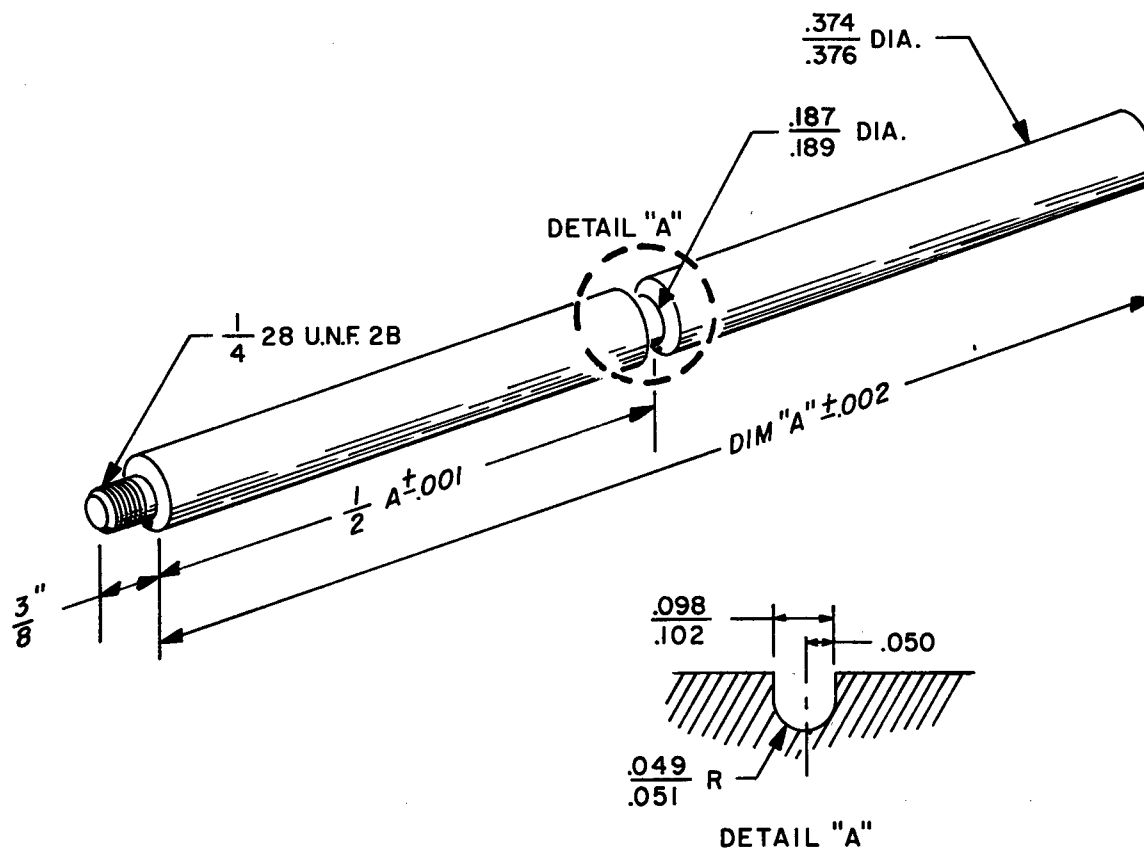
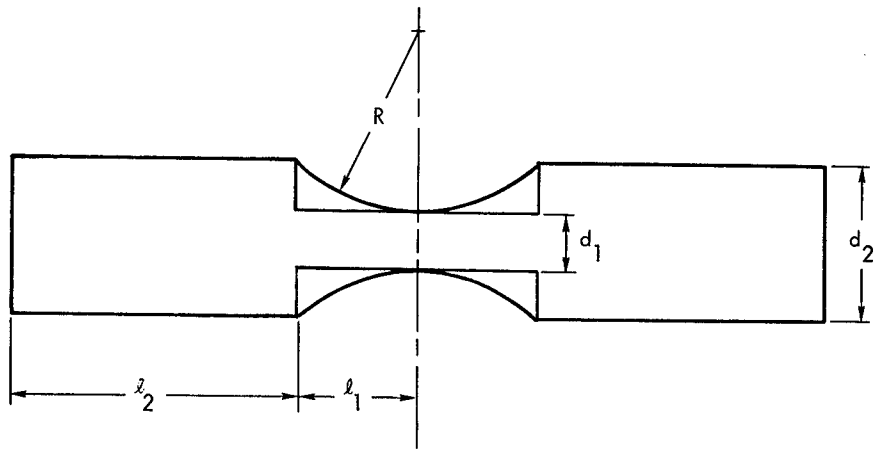


FIGURE 4 - NOTCHED HIGH FREQUENCY FATIGUE SPECIMEN



$$\left(\frac{d_2}{d_1}\right)^2 = \text{AREA RATIO}$$

$\frac{l_1}{\lambda}$ AND $\frac{l_2}{\lambda}$ ARE RELATIVE LENGTHS

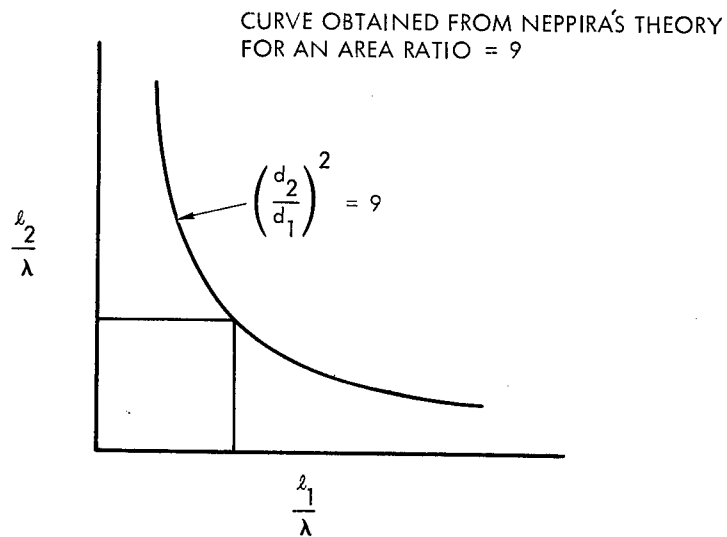
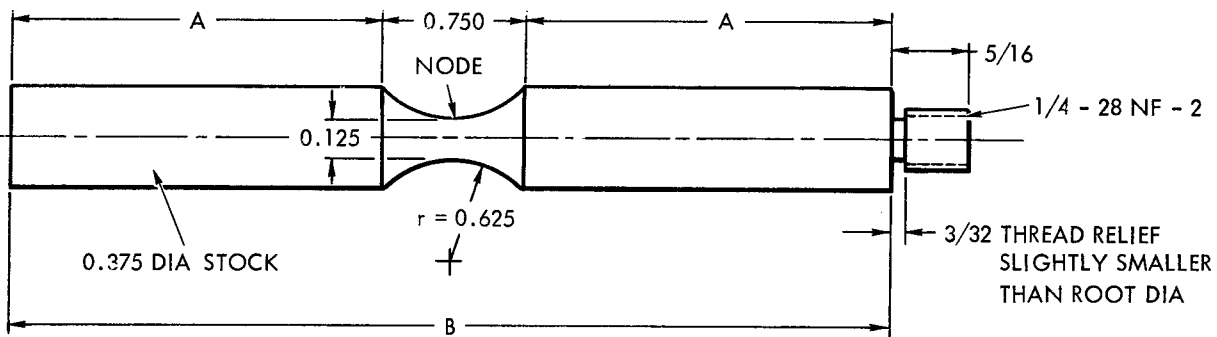


FIGURE 5 - BASIC APPROACH FOR THE DESIGN OF DUMB-BELL SHAPED FATIGUE SPECIMEN



DECIMALS ±0.001
 FRACTIONS ±0.010
 FINISH # 125 UNLESS NOTED

NOTE: 0.625 r REDUCED AREA TO BE GROUND
 AND POLISHED TO 16 RMS MINIMUM

ALL DIMENSIONS ARE IN INCHES

TYPICAL ROOM TEMPERATURE DIMENSIONS

MATERIAL	DIMENSION A	DIMENSION B
316 STAINLESS STEEL	1.812	4.375
1100-0 ALUMINUM	1.855	4.460

FIGURE 6 - DUMB-BELL SHAPED HIGH FREQUENCY FATIGUE SPECIMEN

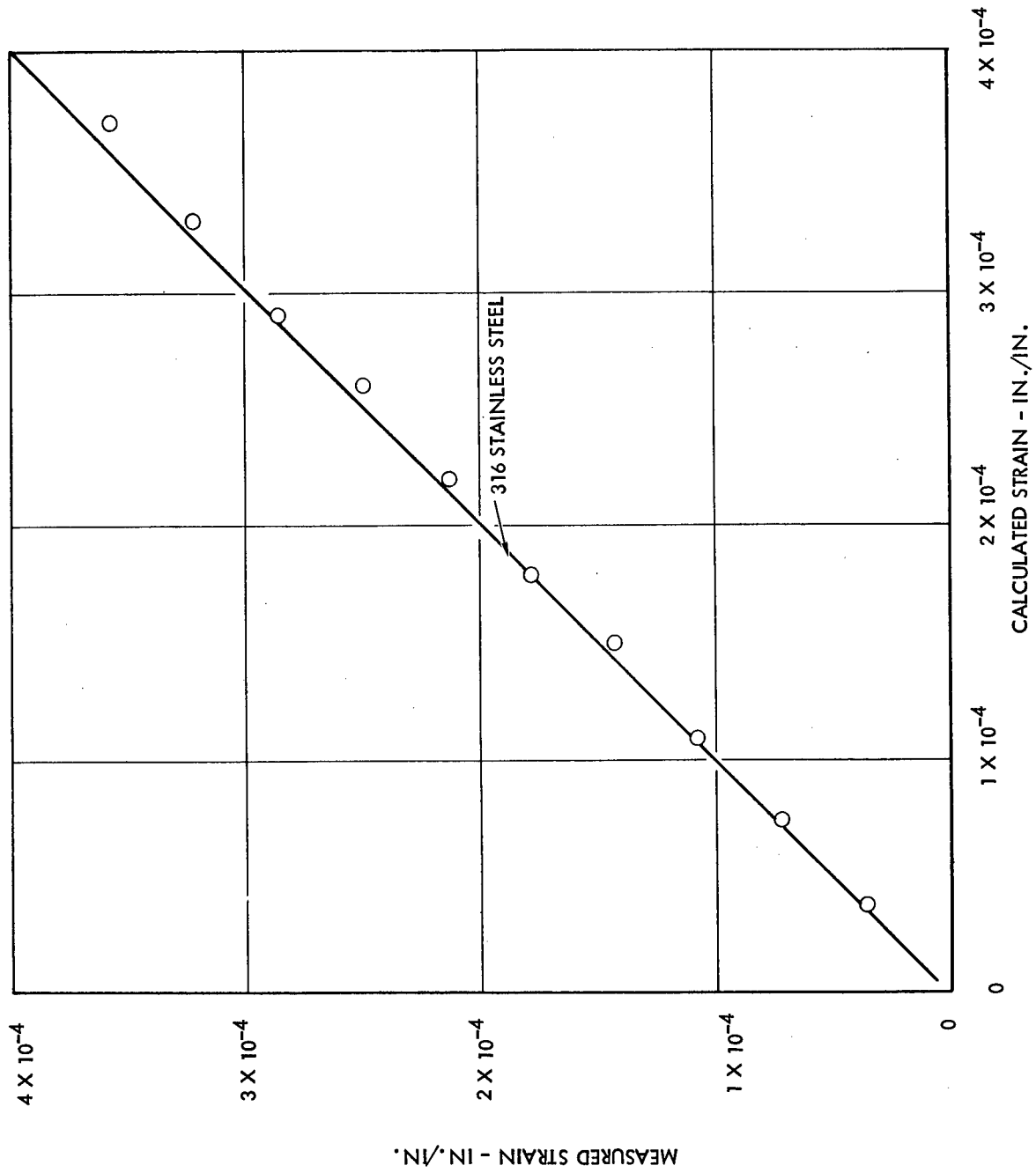


FIGURE 7 - COMPARISON OF THEORETICAL STRAIN AND MEASURED STRAIN FOR DUMB-BELL SHAPED FATIGUE SPECIMENS

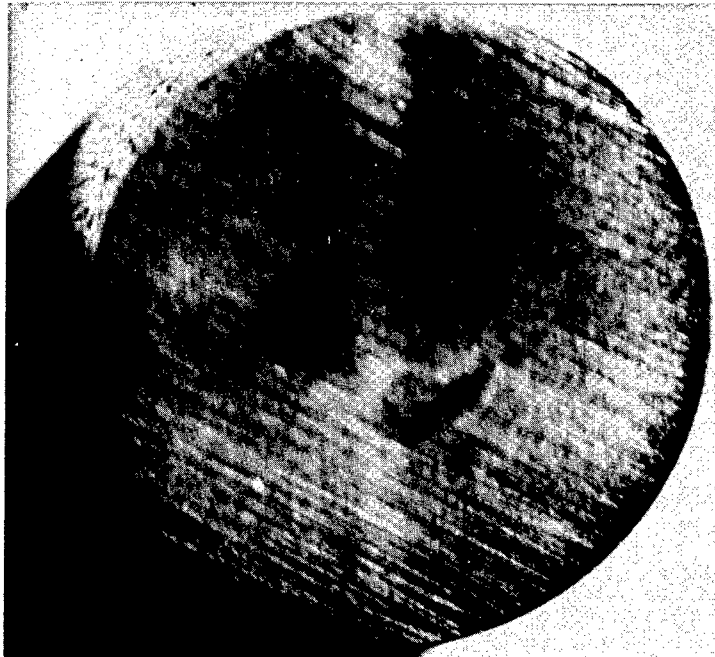
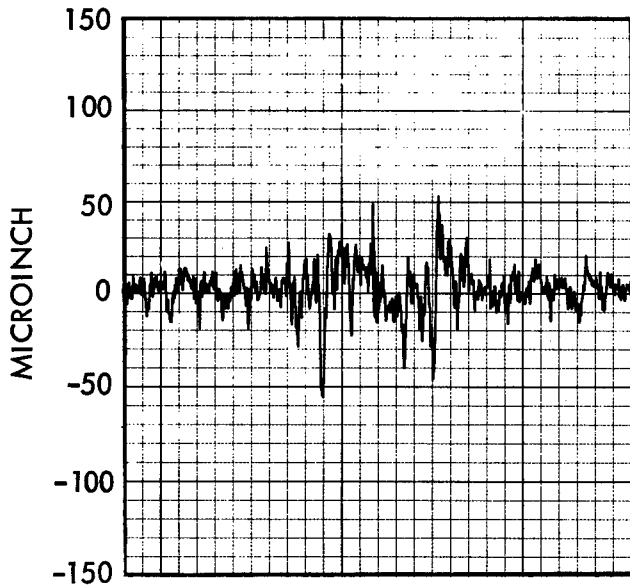
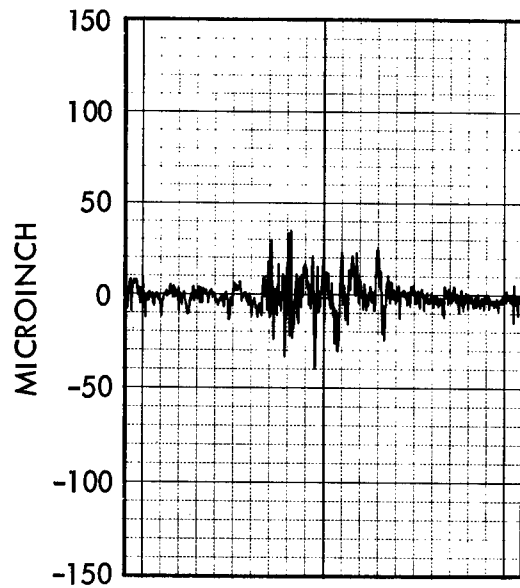


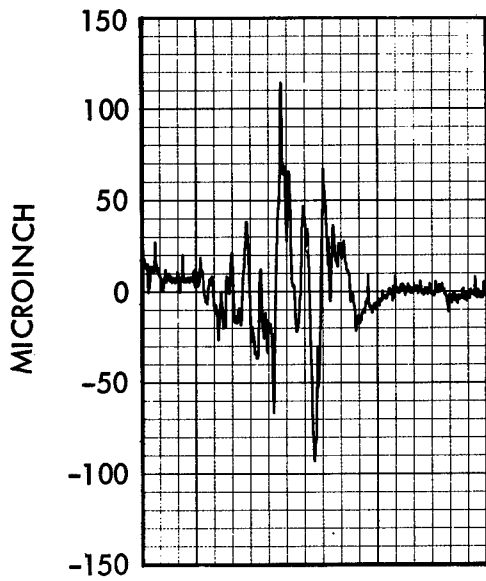
FIGURE 8 - 316 STAINLESS STEEL SPECIMEN RUN 20 HOURS AT 150 FT/SEC FOR
 8.3×10^6 IMPACTS TO THRESHOLD



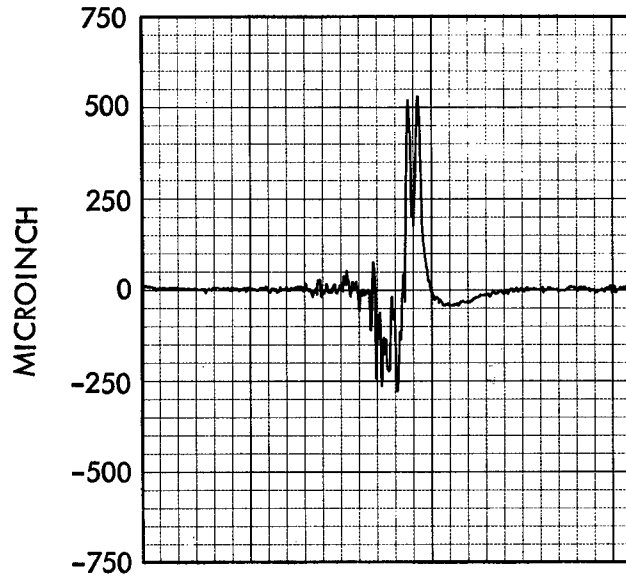
1100-0 ALUMINUM THRESHOLD



316 STAINLESS STEEL THRESHOLD



1100-0 ALUMINUM FRACTURE



316 STAINLESS STEEL FRACTURE

FIGURE 9 - SURFACE ROUGHNESS PROFILE AT THRESHOLD AND AT FRACTURE

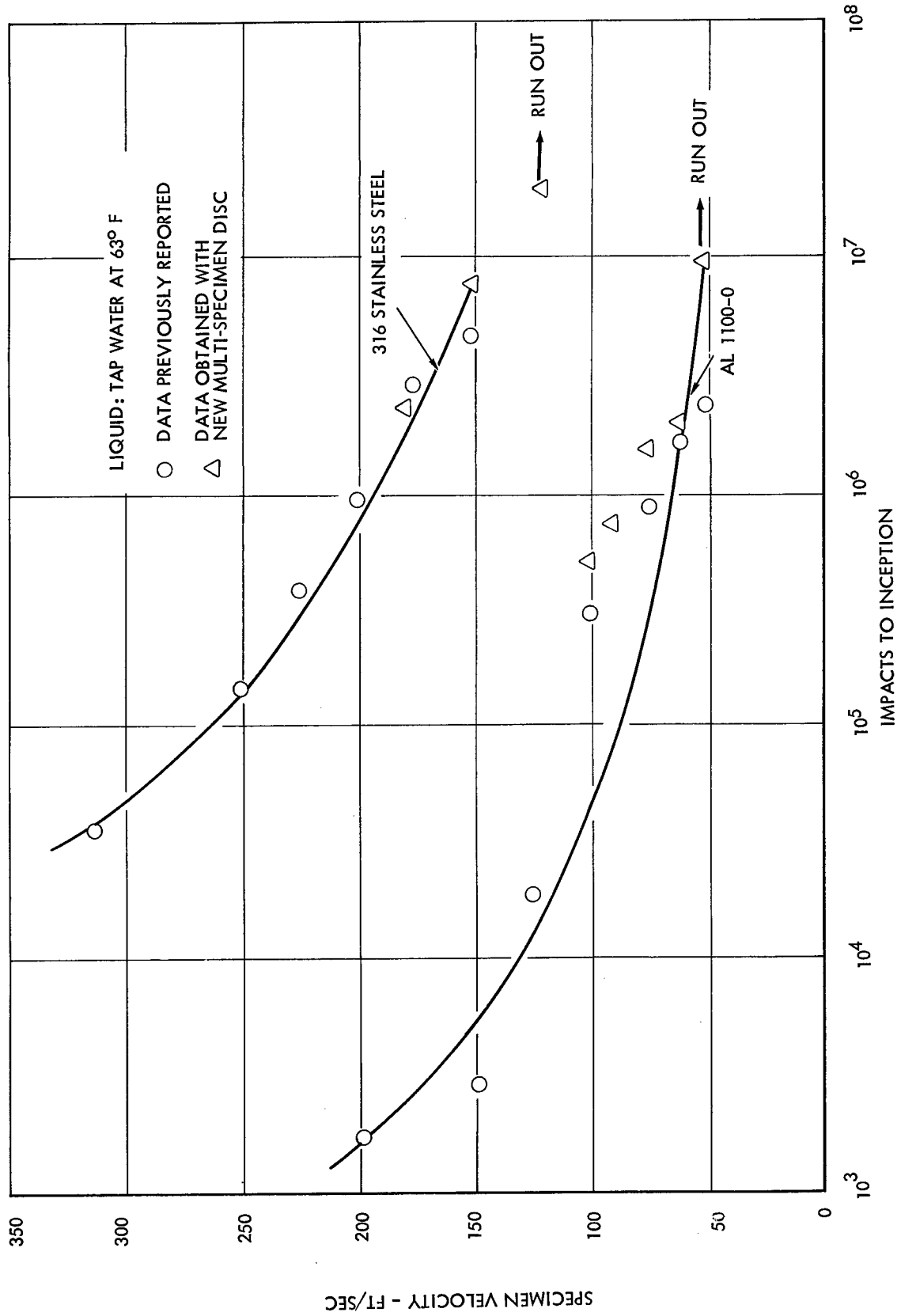


FIGURE 10 - RELATIONSHIP BETWEEN IMPACT SPEED AND THE NUMBER OF IMPACTS UNTIL INITIAL PLASTIC DENTS ARE OBTAINED ON 316 STAINLESS STEEL AND ON 1100-0 ALUMINUM

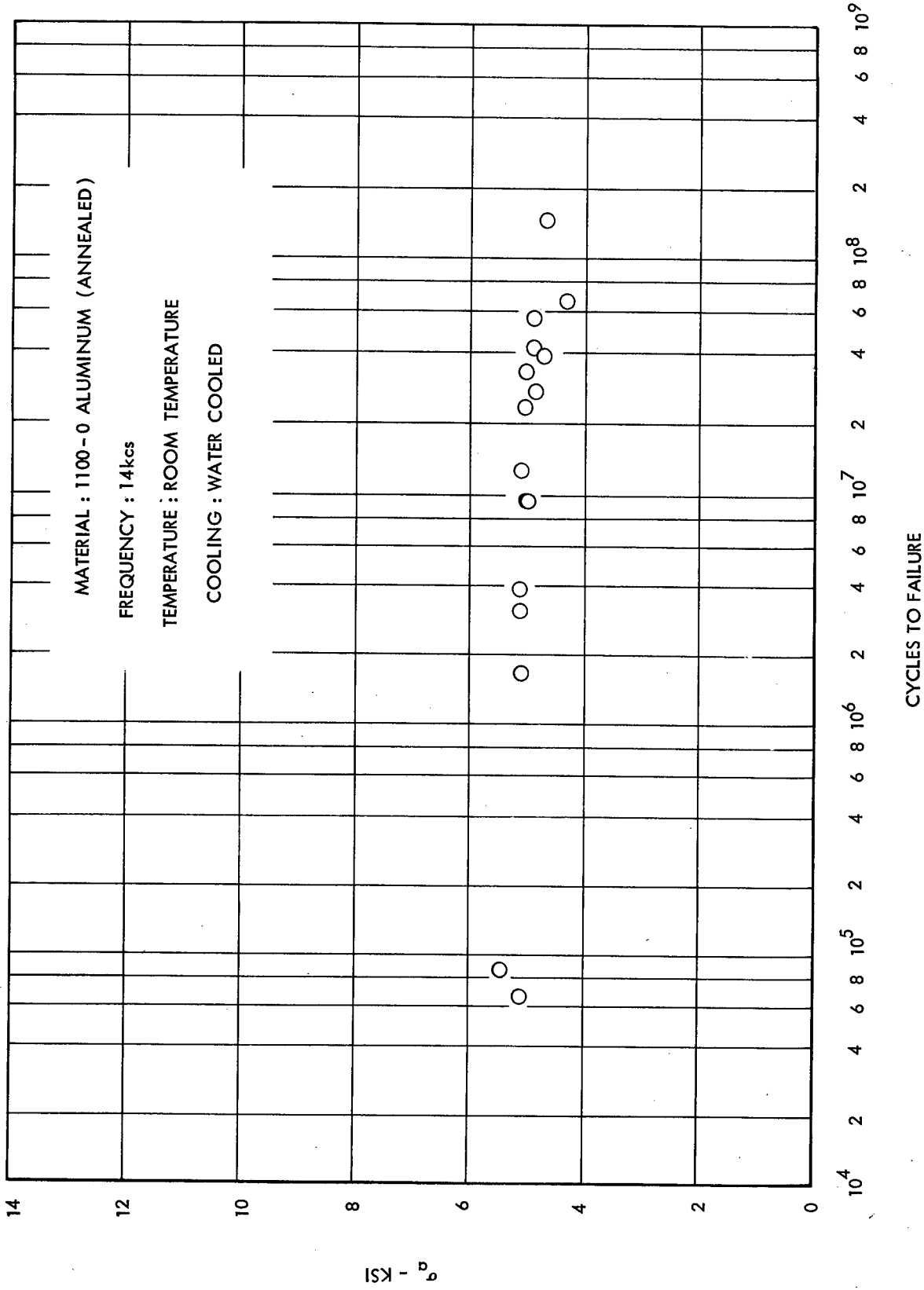


FIGURE 11 - 1100-0 ALUMINUM FATIGUE DATA AT HIGH FREQUENCY - RELATIONSHIP BETWEEN STRESS AMPLITUDE AND NUMBER OF CYCLES TO FRACTURE

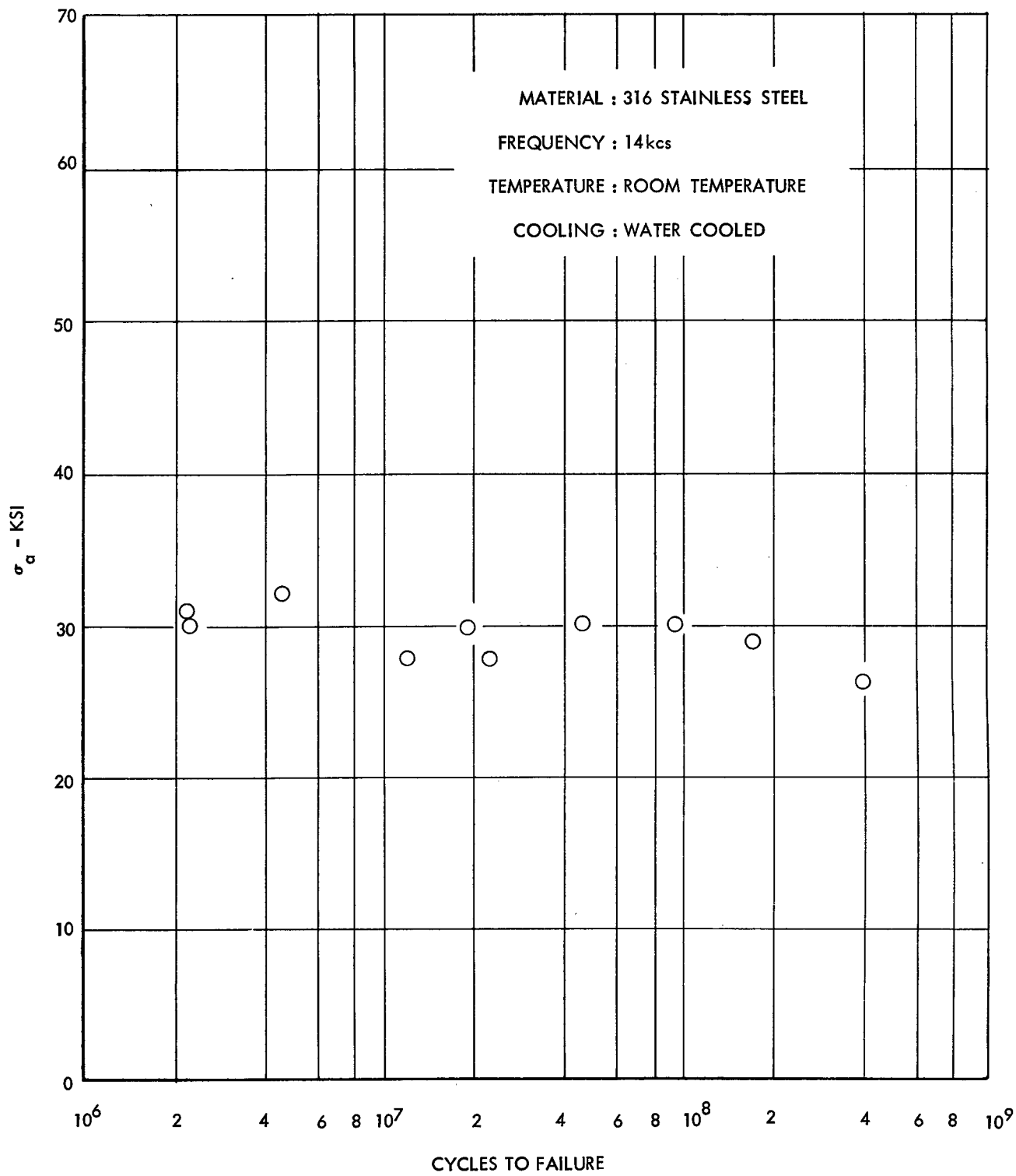


FIGURE 12 - 316 STAINLESS STEEL FATIGUE DATA AT HIGH FREQUENCY - RELATIONSHIP BETWEEN STRESS AMPLITUDE AND NUMBER OF CYCLES TO FRACTURE

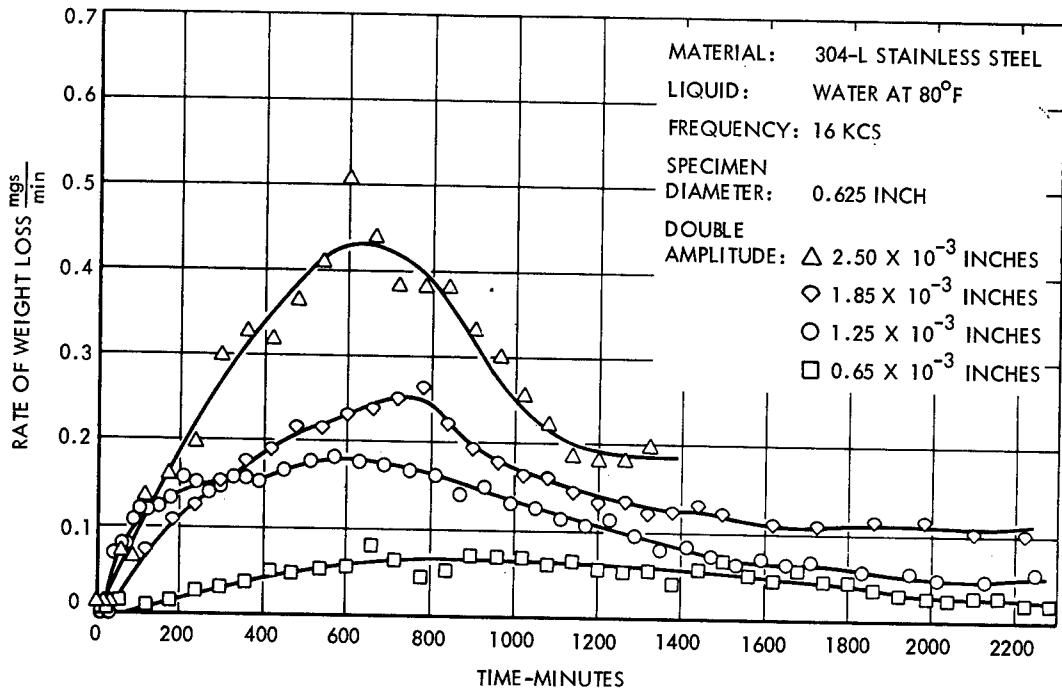


FIGURE 13 - EFFECT OF TIME ON CAVITATION DAMAGE RATE FOR VARIOUS AMPLITUDES (REFERENCE 9)

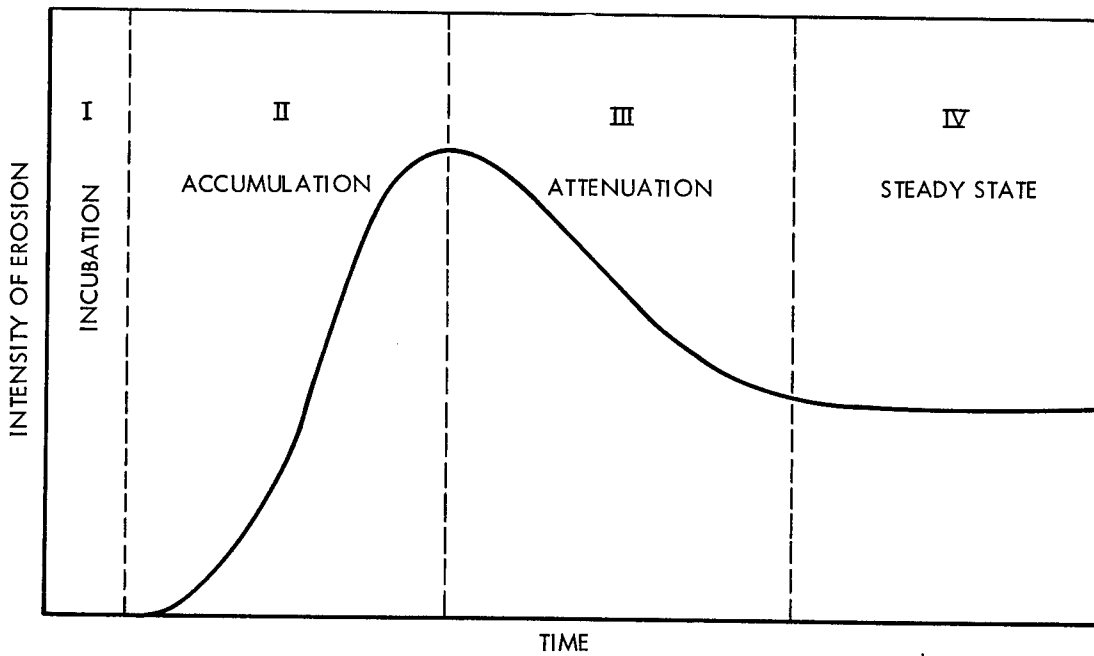


FIGURE 14 - EFFECT OF TIME ON INTENSITY OF EROSION

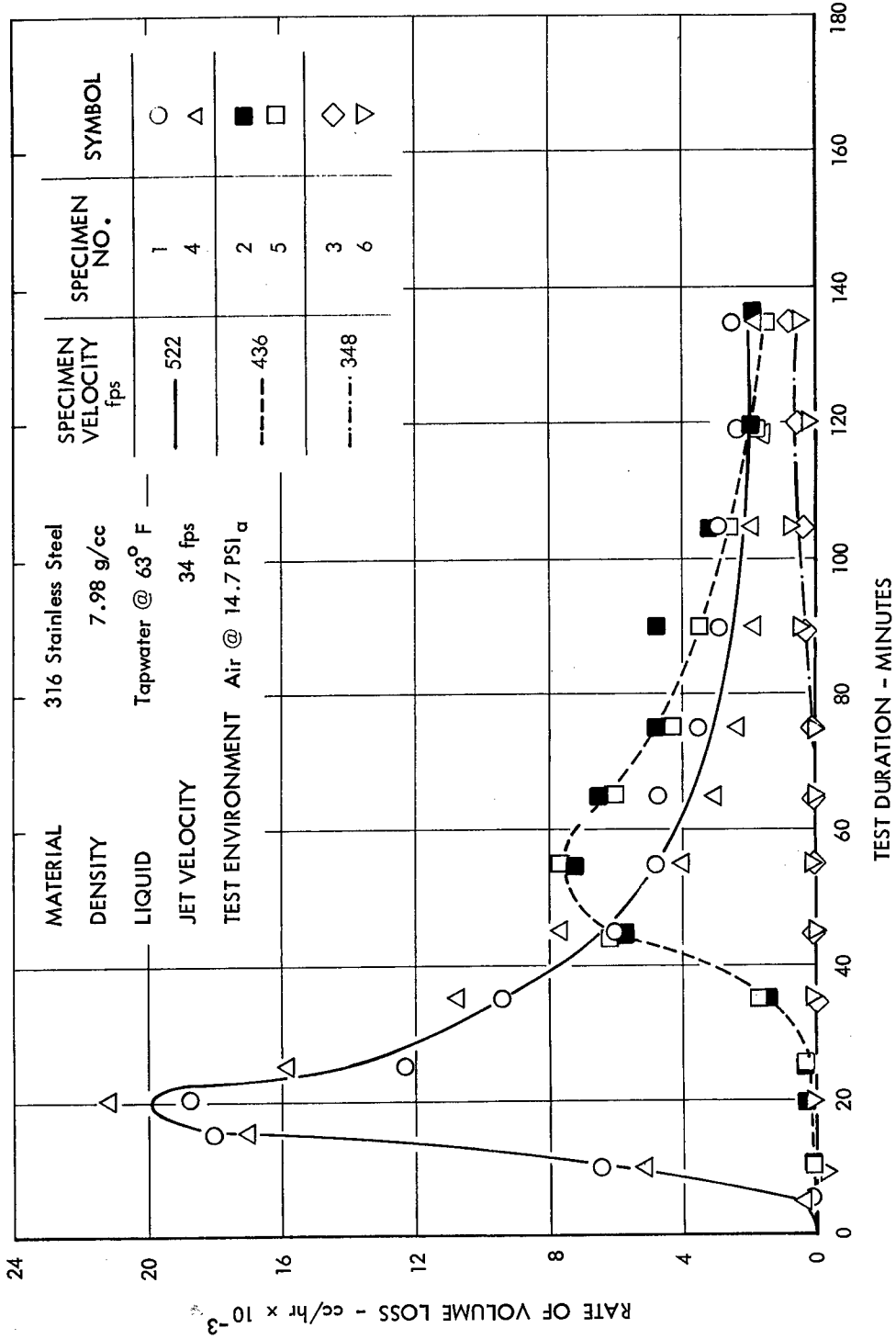


FIGURE 15 - RATE OF VOLUME LOSS AS A FUNCTION OF TIME AT THREE VELOCITIES FOR 316 STAINLESS STEEL

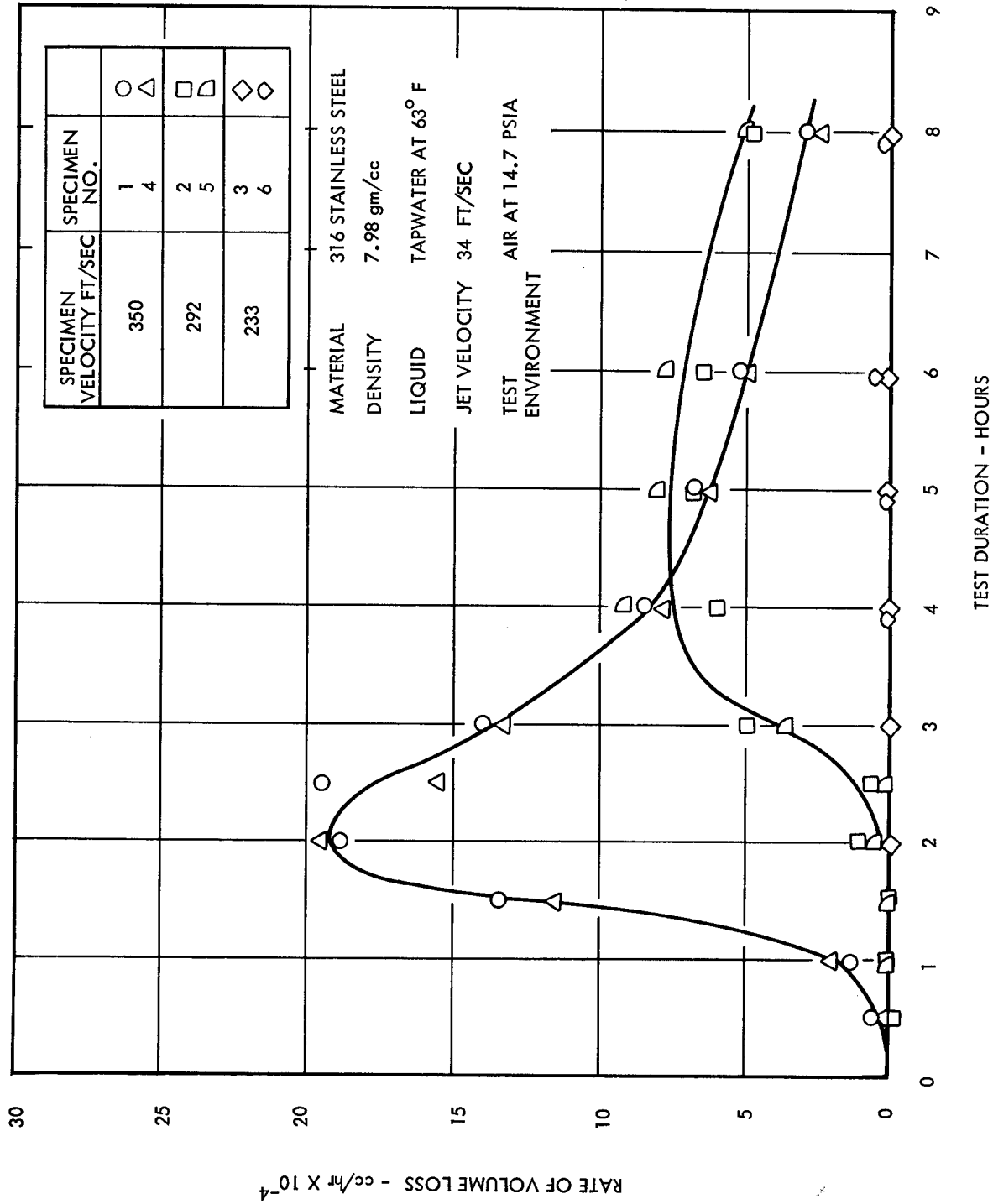


FIGURE 16 - RATE OF VOLUME LOSS AS A FUNCTION OF TIME AT THREE VELOCITIES FOR 316 STAINLESS STEEL

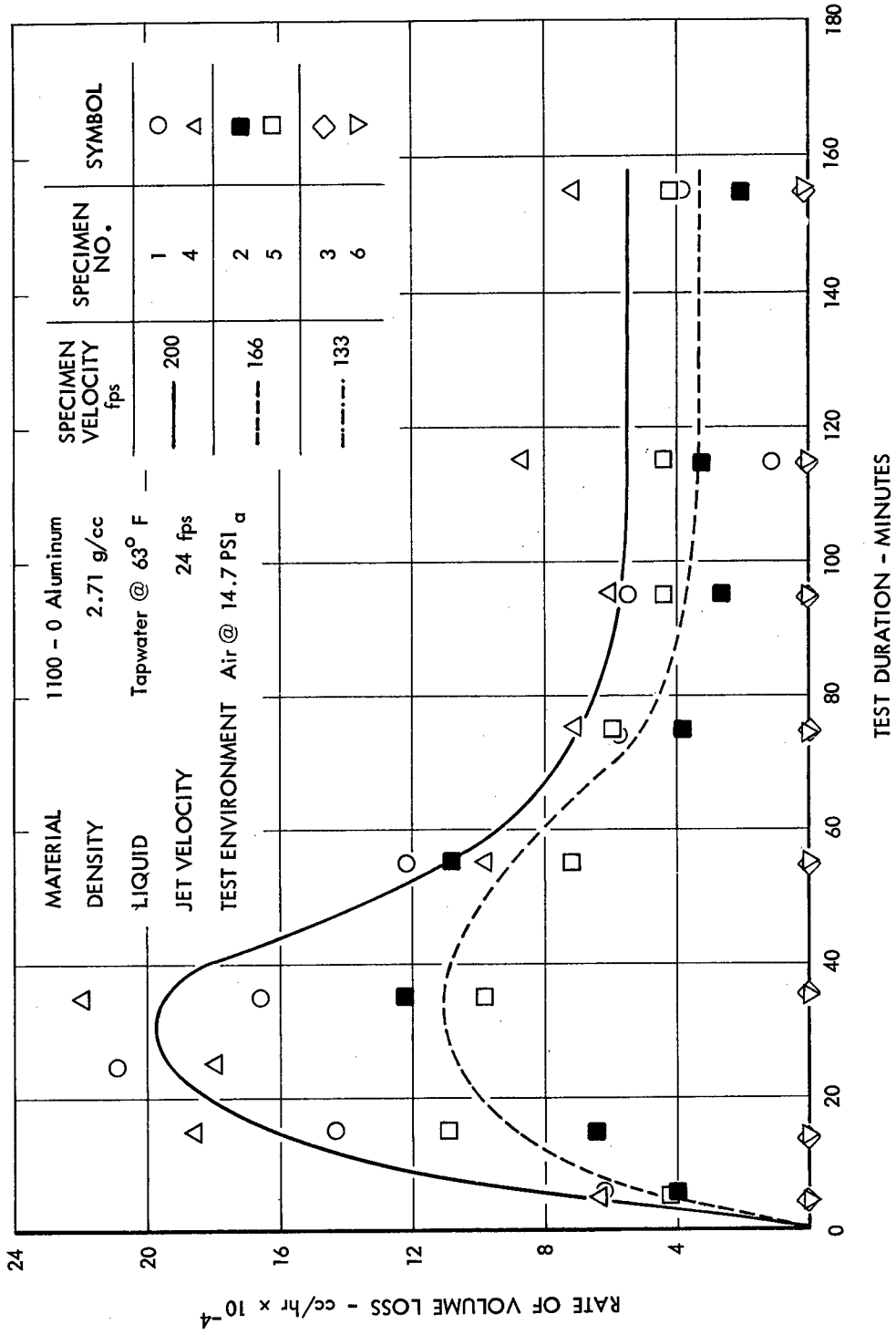


FIGURE 17 - RATE OF VOLUME LOSS AS A FUNCTION OF TIME AT THREE VELOCITIES FOR 1100-0 ALUMINUM

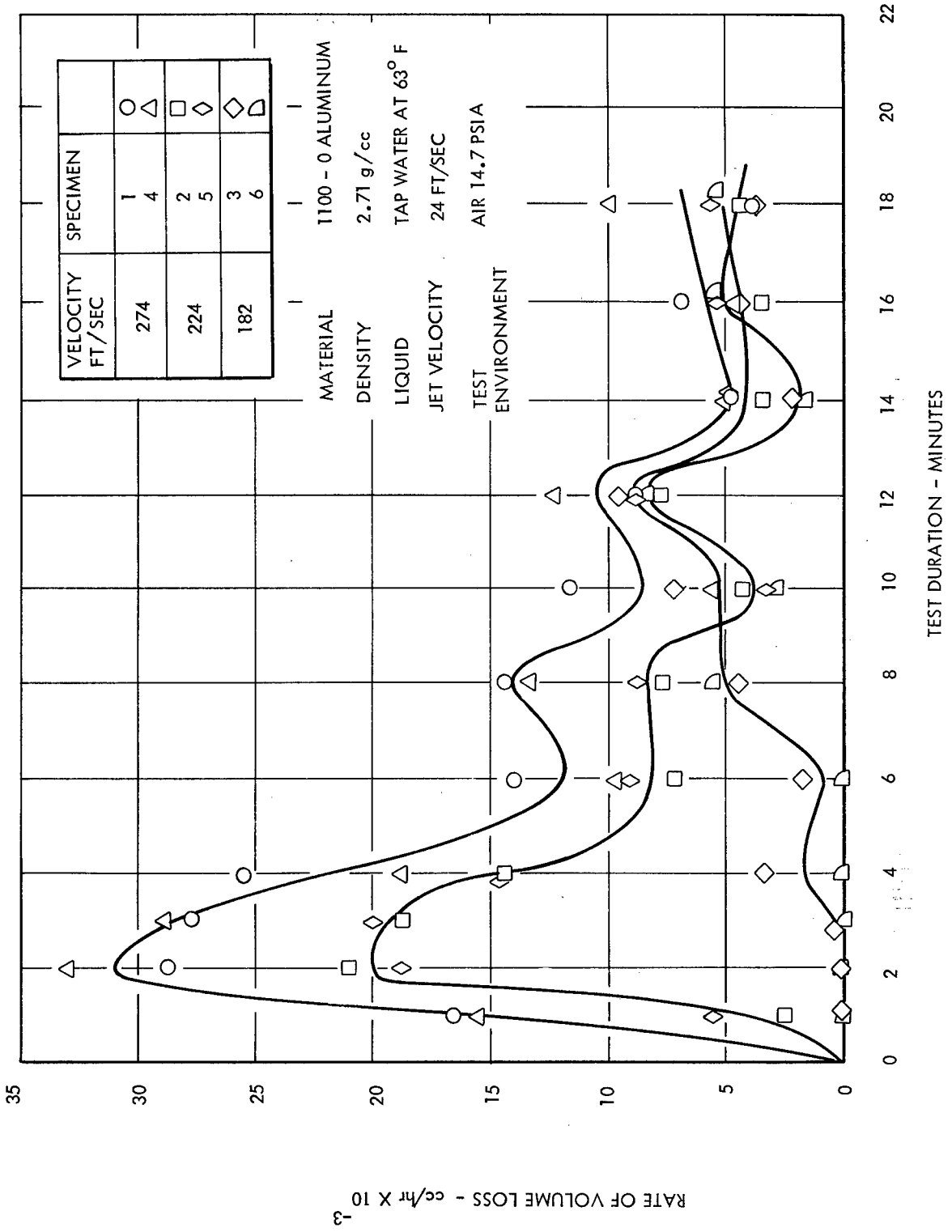


FIGURE 18 - RATE OF VOLUME LOSS AS A FUNCTION OF TIME AT THREE VELOCITIES FOR 1100-0 ALUMINUM

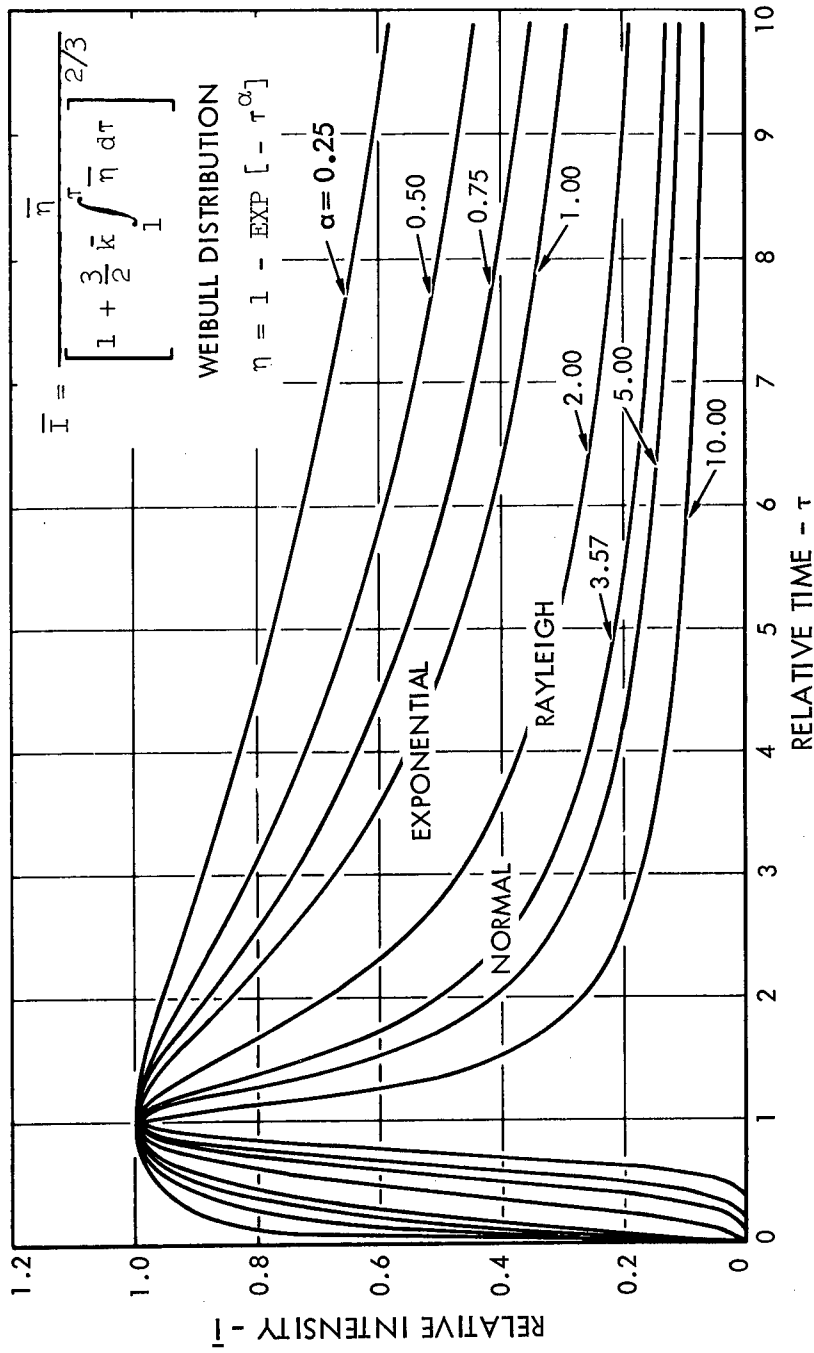


FIGURE 19 - THEORETICAL PREDICTION OF THE EFFECT OF TIME ON INTENSITY OF EROSION WHEN $n = 2$

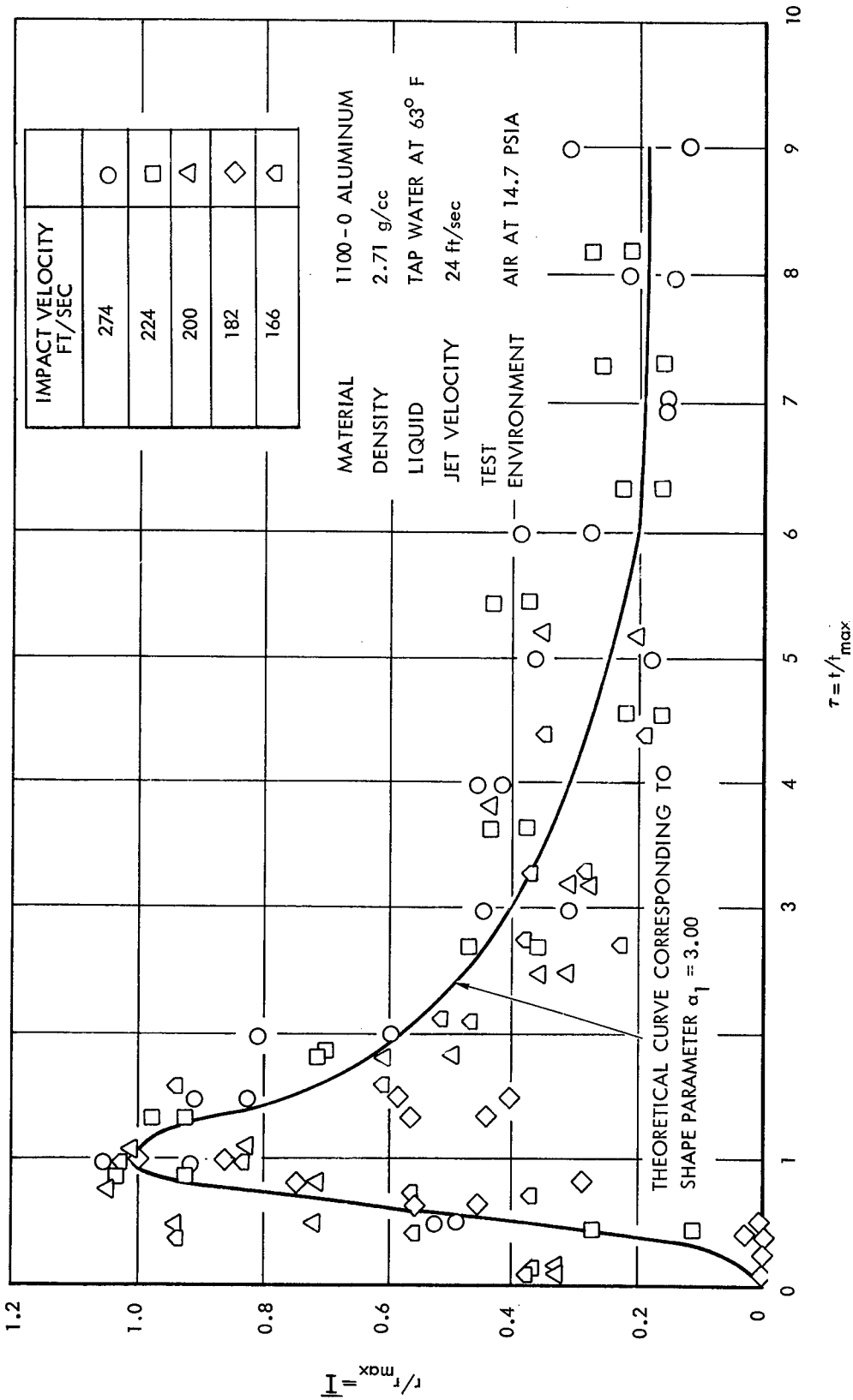


FIGURE 20 - COMPARISON OF EXPERIMENTAL RESULTS WITH THE EROSION THEORY FOR 1100-0 ALUMINUM

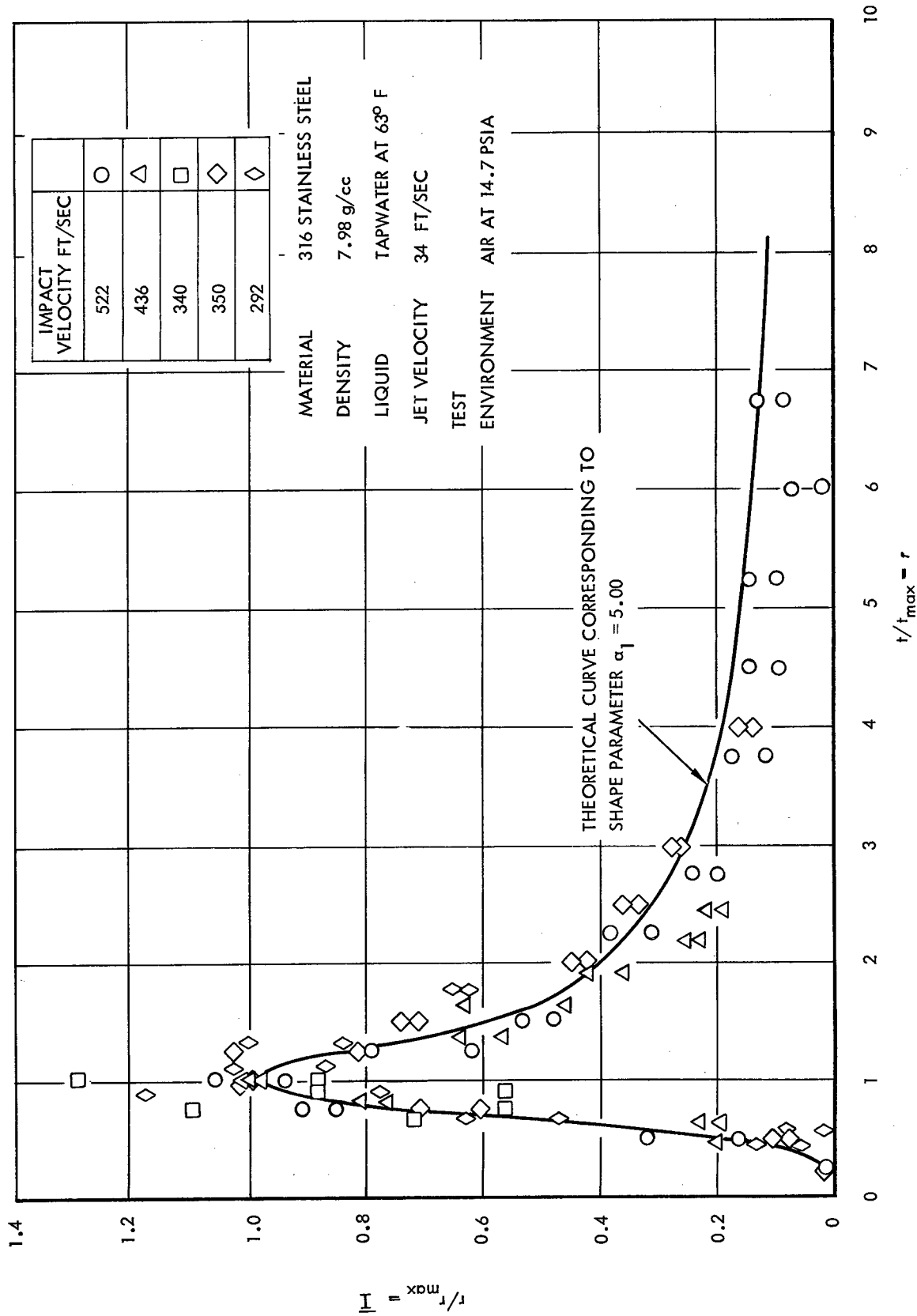


FIGURE 21 - COMPARISON OF EXPERIMENTAL RESULTS WITH THE EROSION THEORY FOR 316 STAINLESS STEEL

MATERIAL : 1100-0 ALUMINUM
 SAMPLE SIZE : 29
 FREQUENCY OF TEST : 14.2 kcs

STRESS LEVEL : 5000 psi (Axial Push-Pull)
 TEMPERATURE : ROOM TEMPERATURE
 ENVIRONMENT : WATER COOLED

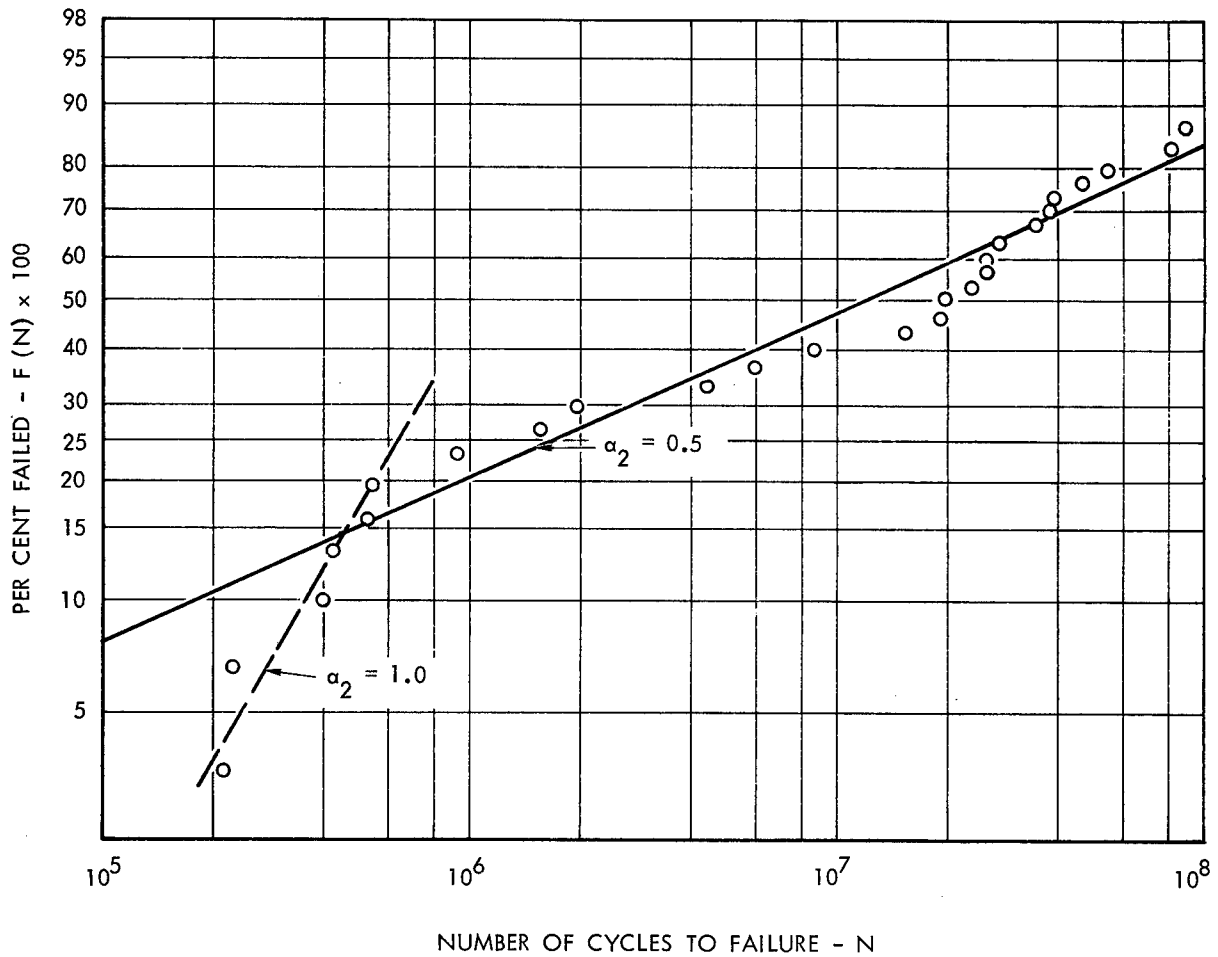


FIGURE 22 - WEIBULL DISTRIBUTION FOR HIGH FREQUENCY FATIGUE OF 1100-0 ALUMINUM AT ROOM TEMPERATURE

MATERIAL	:	316 STAINLESS STEEL	STRESS LEVEL	:	30,000 psi (Axial Push - Pull)
SAMPLE SIZE	:	20	TEMPERATURE	:	ROOM TEMPERATURE
FREQUENCY OF TEST	:	14.2 kcs	ENVIRONMENT	:	WATER COOLED

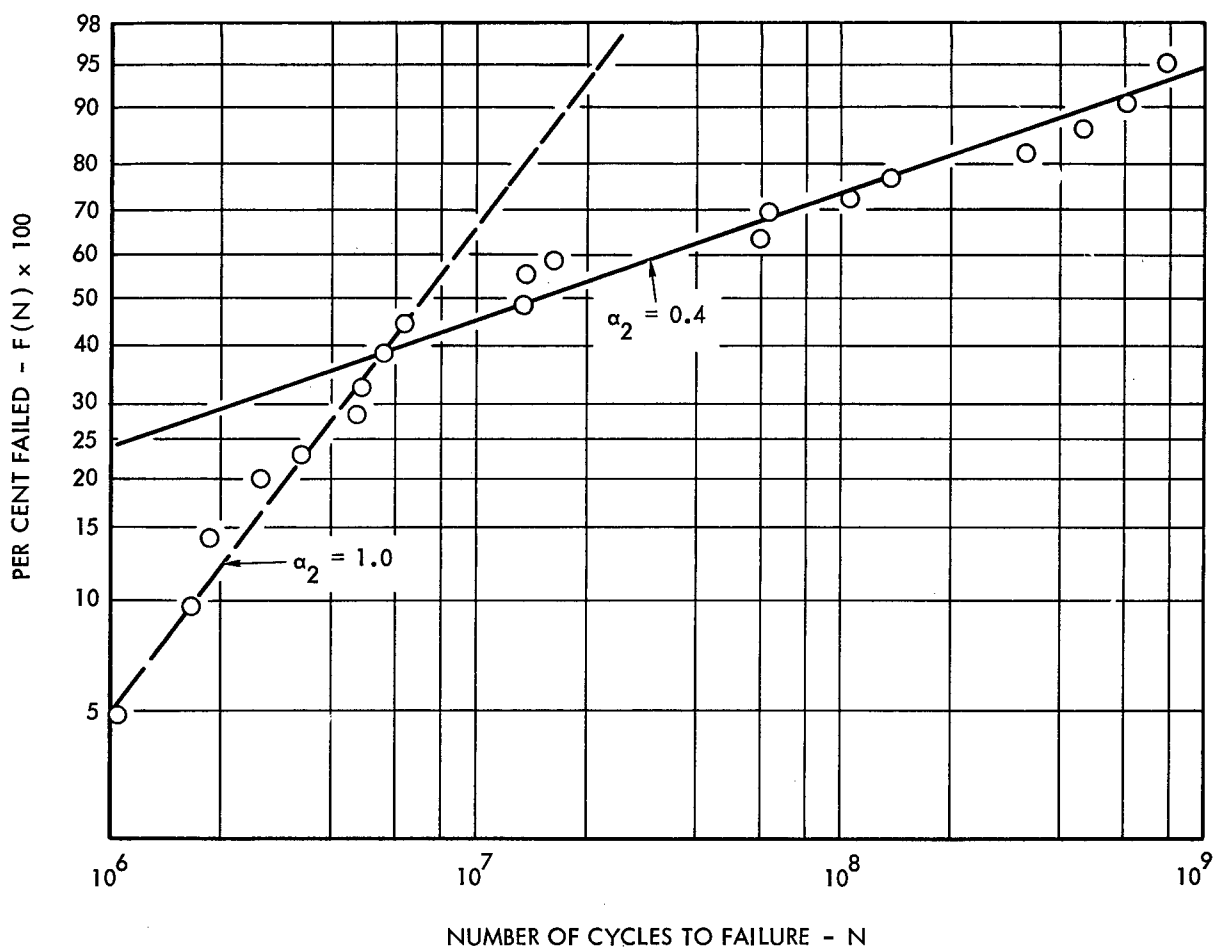


FIGURE 23 - WEIBULL DISTRIBUTION FOR HIGH FREQUENCY FATIGUE OF 316 STAINLESS STEEL AT ROOM TEMPERATURE

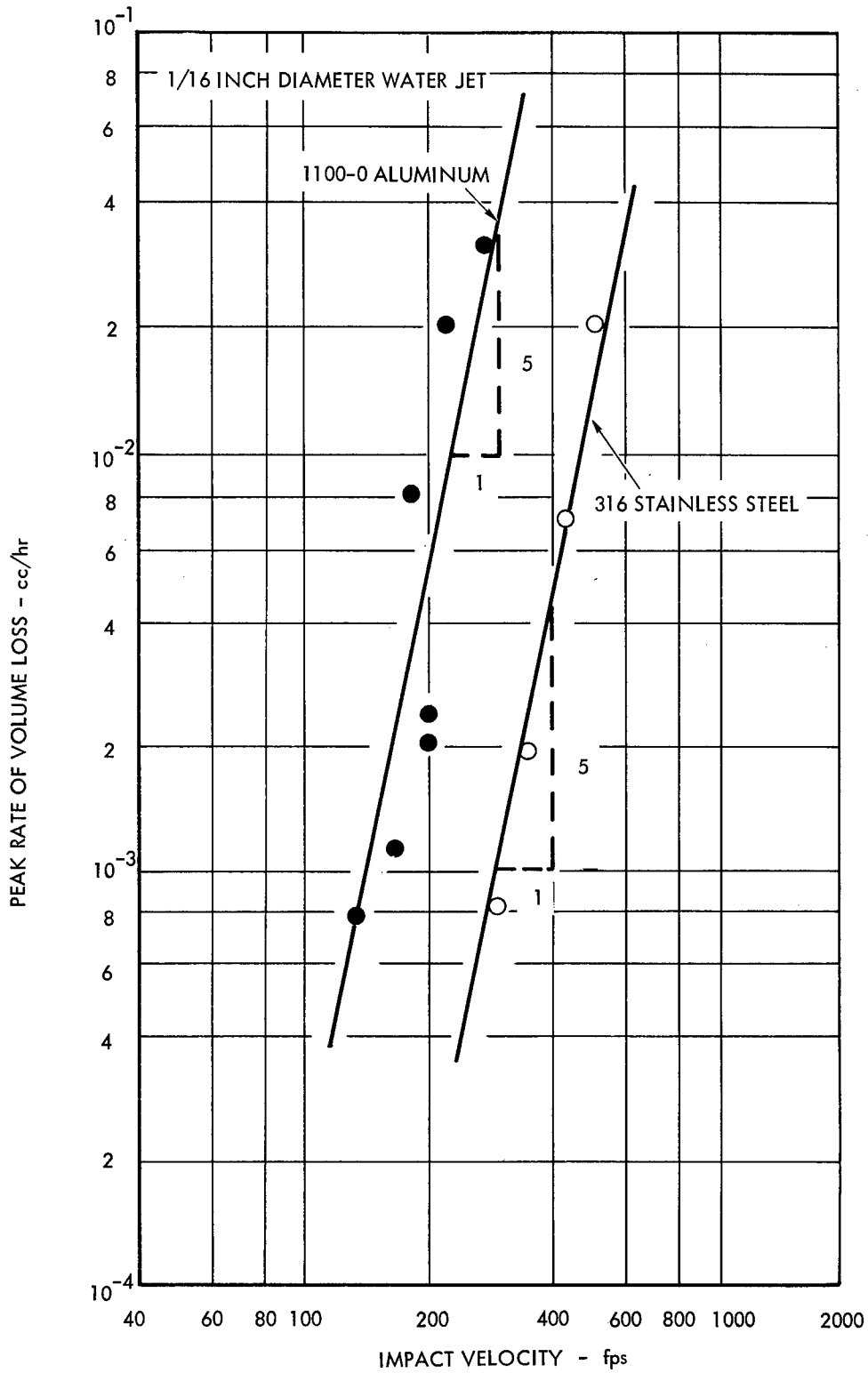


FIGURE 24 - RELATIONSHIP BETWEEN PEAK RATE OF VOLUME LOSS AND THE IMPACT VELOCITY

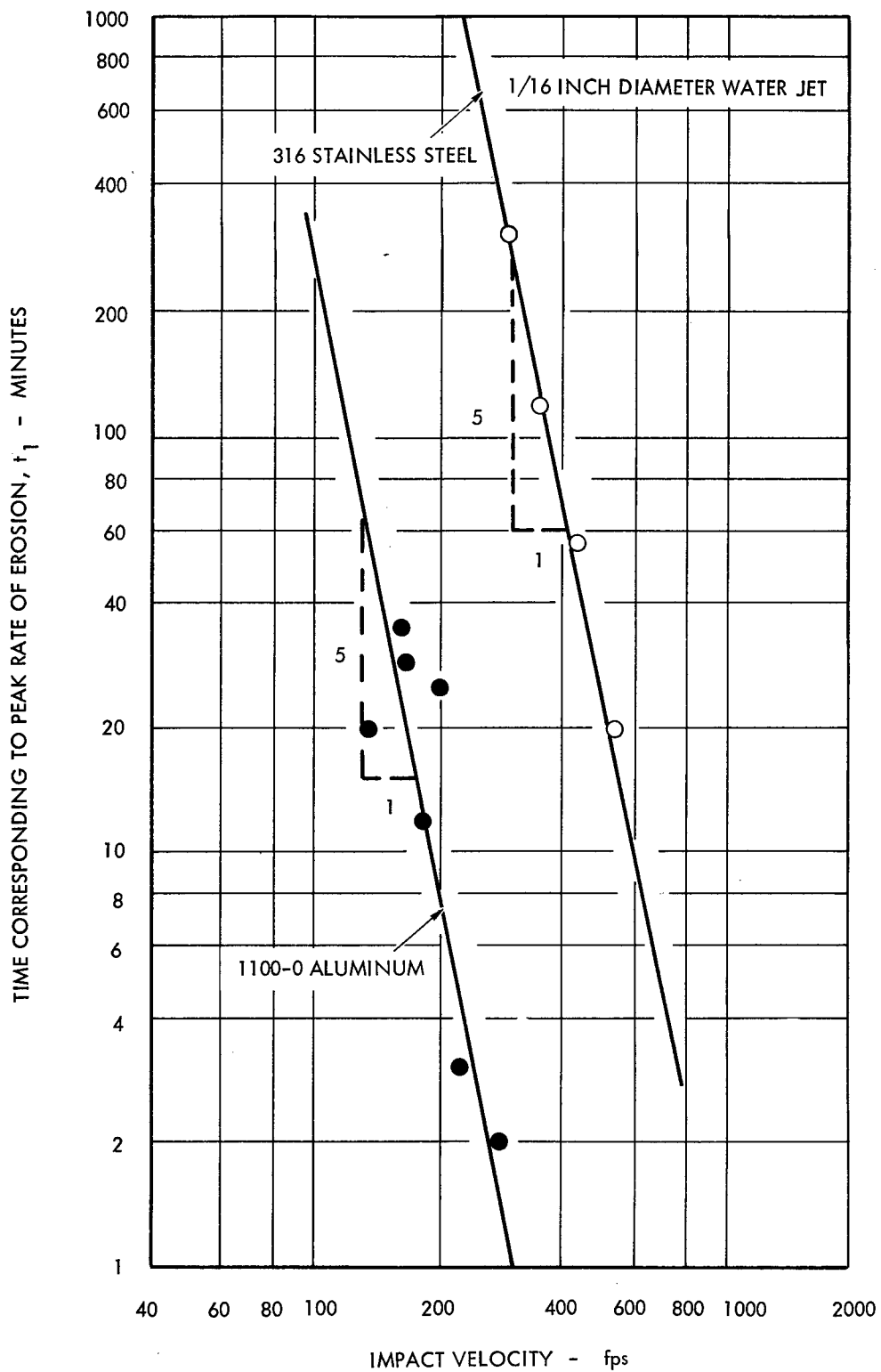


FIGURE 25 - RELATIONSHIP BETWEEN THE TIME AT WHICH PEAK RATE OF VOLUME LOSS IS OBSERVED AND THE IMPACT VELOCITY

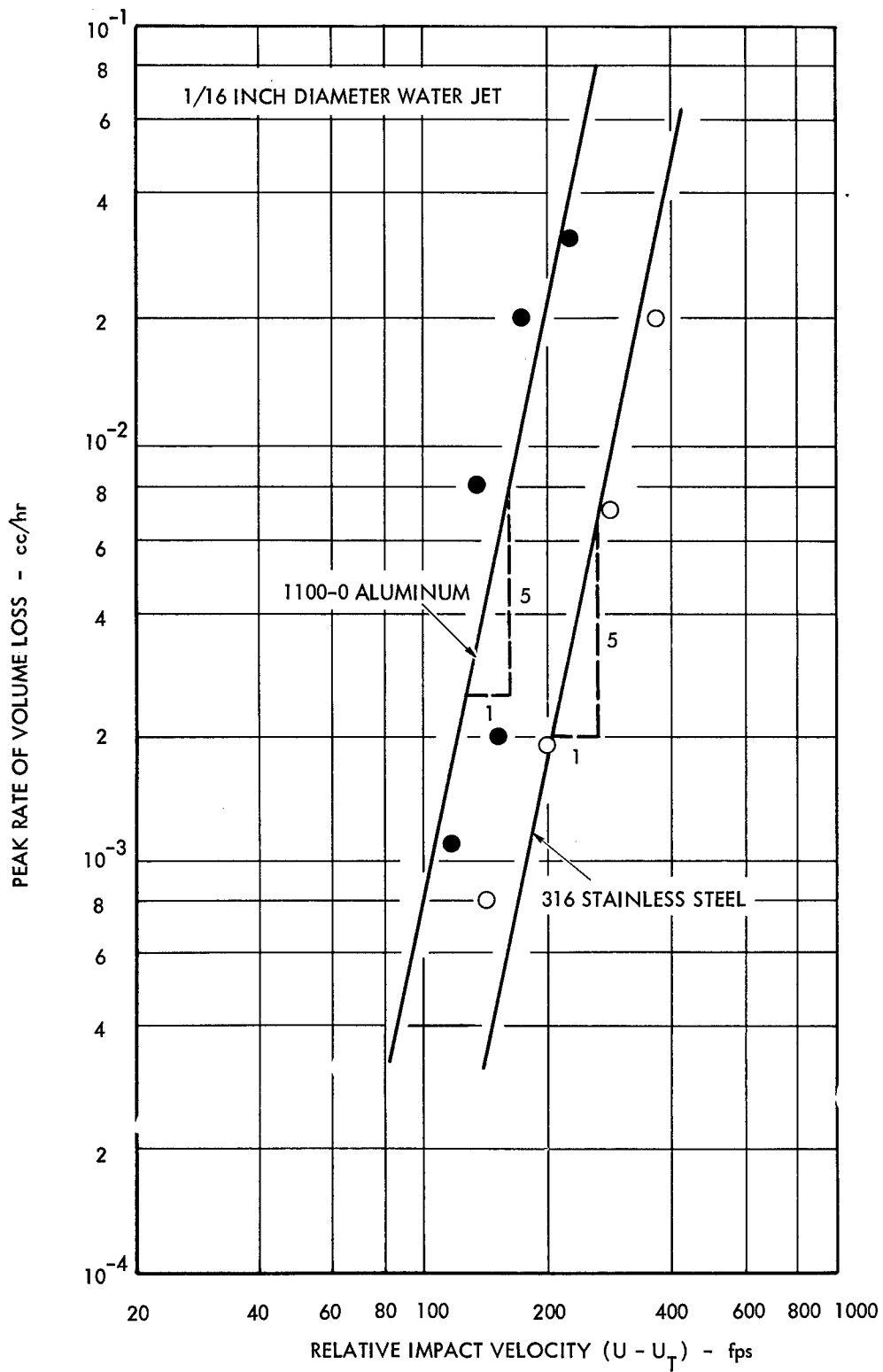
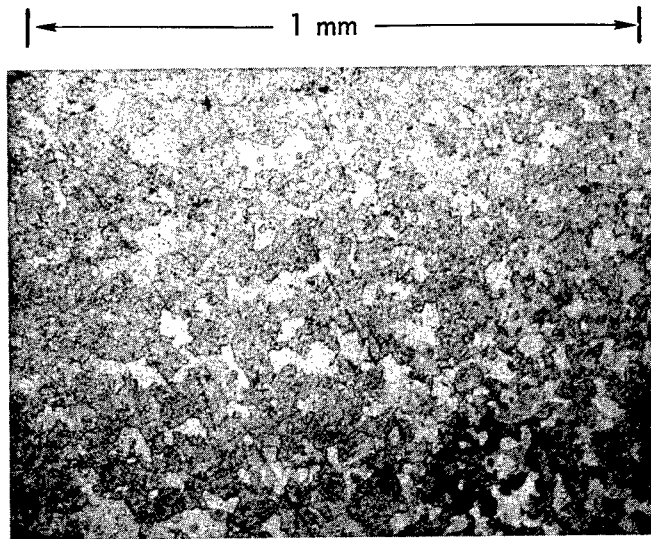
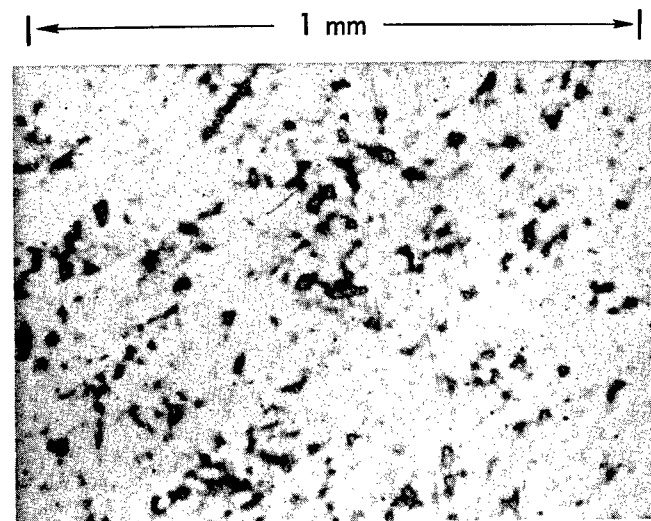


FIGURE 26 - RELATIONSHIP BETWEEN THE RELATIVE IMPACT VELOCITY AND THE RATE OF VOLUME LOSS

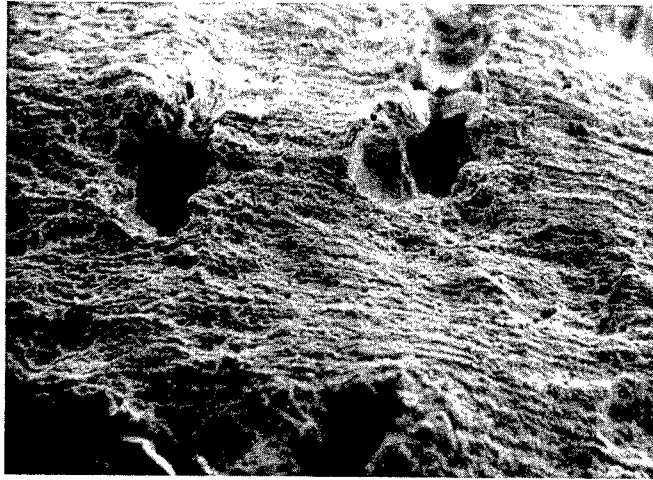


1100-0 ALUMINUM

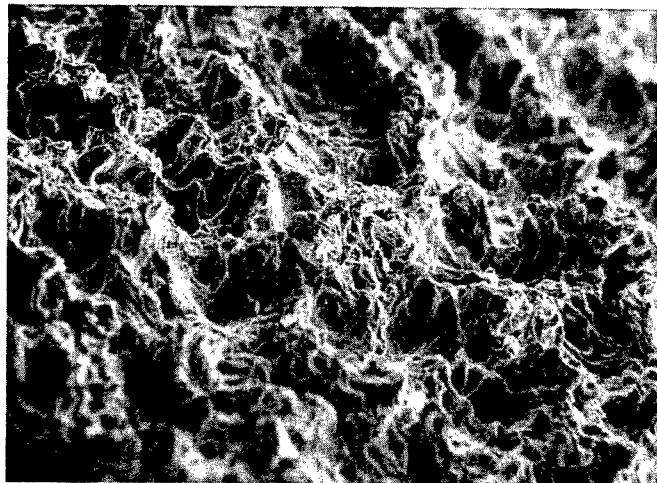


316 STAINLESS STEEL

FIGURE 27 - MICROPHOTOGRAPHS OF THE TEST MATERIALS
SHOWING STRUCTURE



LIQUID IMPACT EROSION OF 1100-0 ALUMINUM
IMPINGEMENT VELOCITY 450 fps FOR 3 MINUTES
(MAGNIFICATION: 88X)



CAVITATION EROSION OF 1100-0 ALUMINUM USING THE
MAGNETOSTRICTION DEVICE DRIVING FREQUENCY
14.2 kcs DOUBLE AMPLITUDE 2.0×10^{-3} INCHES FOR
1 MINUTE (MAGNIFICATION: 74X)

FIGURE 28 - COMPARISON OF INDENTATIONS PRODUCED BY MULTIPLE
LIQUID IMPACT EROSION AND BY CAVITATION EROSION -
SCANNING ELECTRON MICROPHOTOGRAPHS

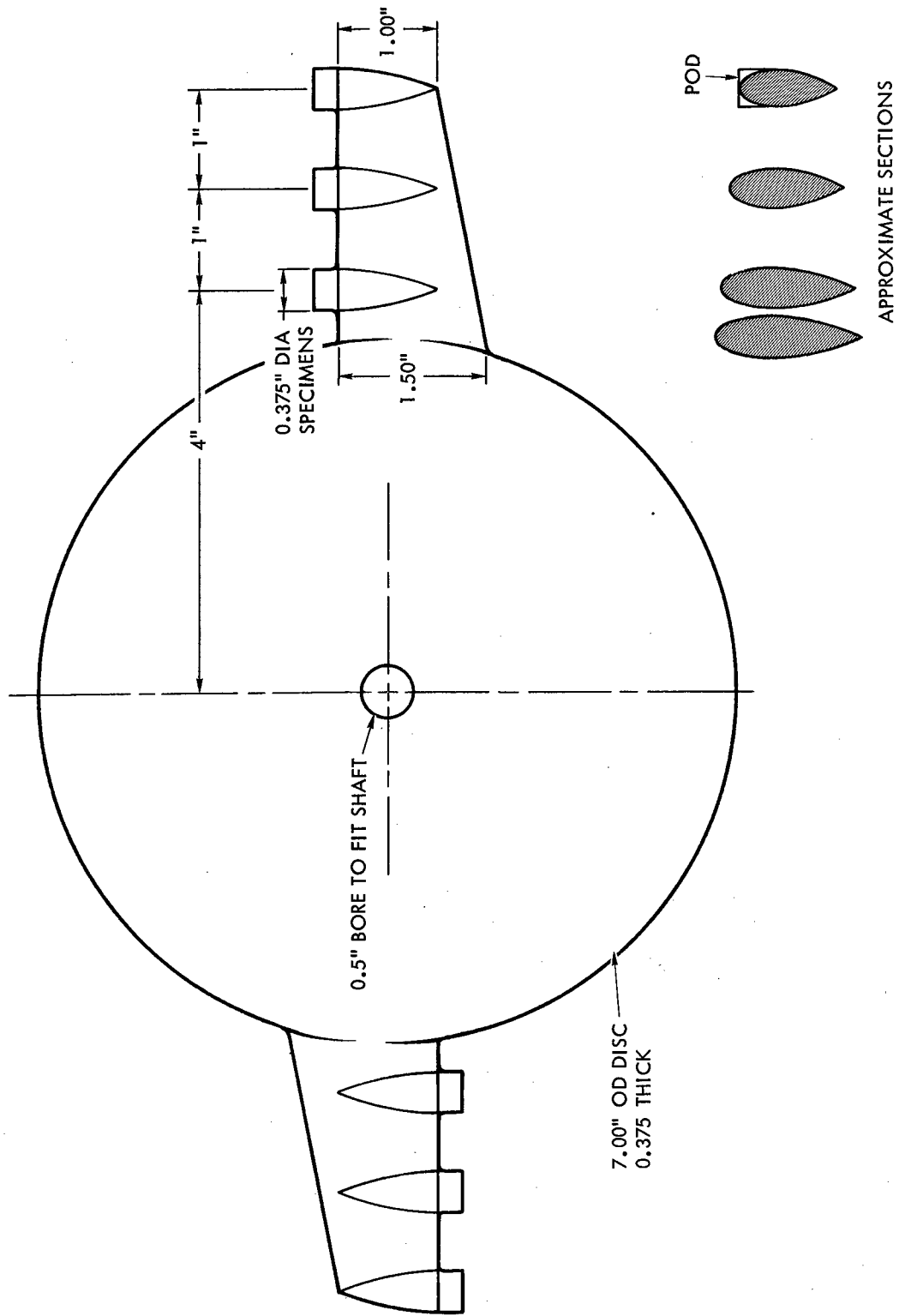
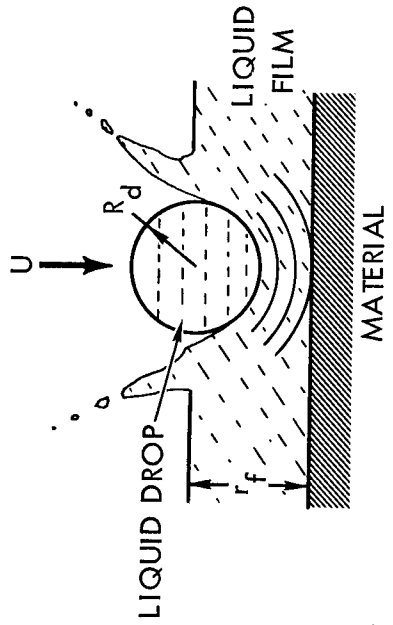
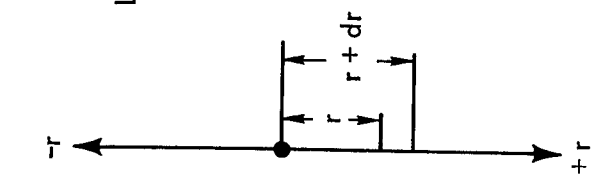


FIGURE 29 - ROTATING DISC CAPABLE OF HOLDING SIX SPECIMENS



- U - DROP VELOCITY
- R_d - RADIUS OF DROP
- r_f - FILM THICKNESS

b. DROP IMPACT EROSION



- R_m - MAXIMUM RADIUS OF BUBBLE
- R_f - FINAL RADIUS OF BUBBLE
- R_p - RADIUS AT WHICH PEAK PRESSURE OCCURS
- r_c - DISTANCE FROM THE ORIGINAL MATERIAL SURFACE TO THE CENTER OF COLLAPSE

a. CAVITATION EROSION

FIGURE 30 - DEFINITION SKETCH

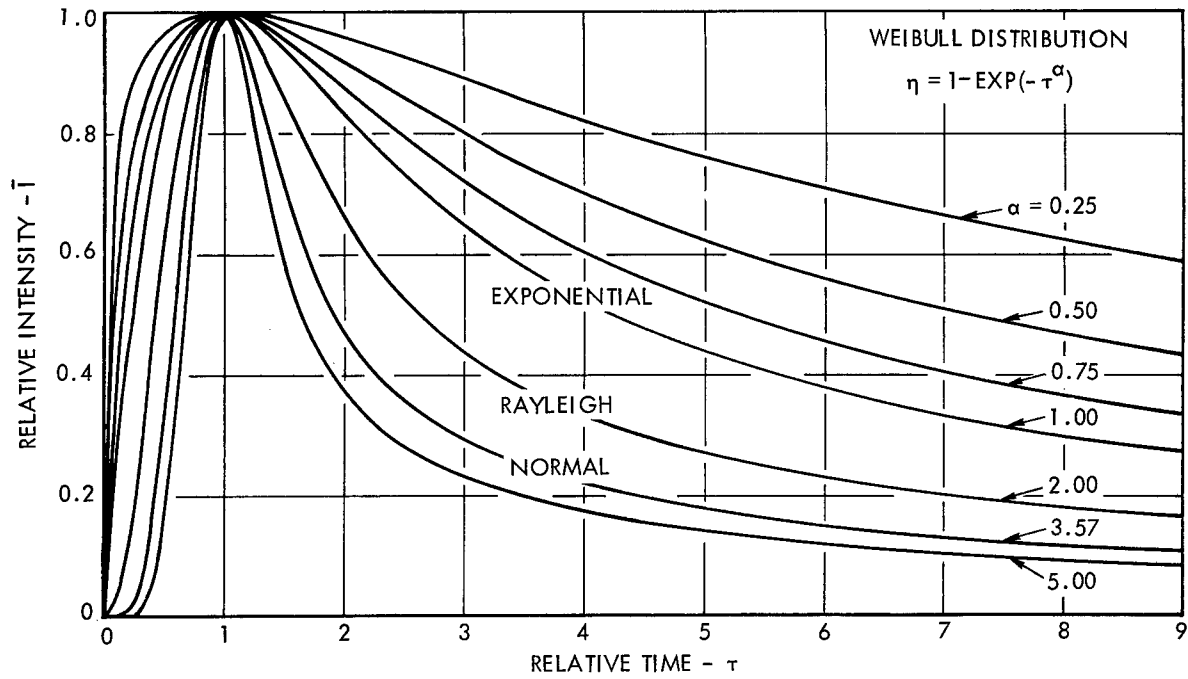


FIGURE 31 - THEORETICAL PREDICTION OF THE EFFECT OF TIME ON INTENSITY OF EROSION WHEN $n = 3$

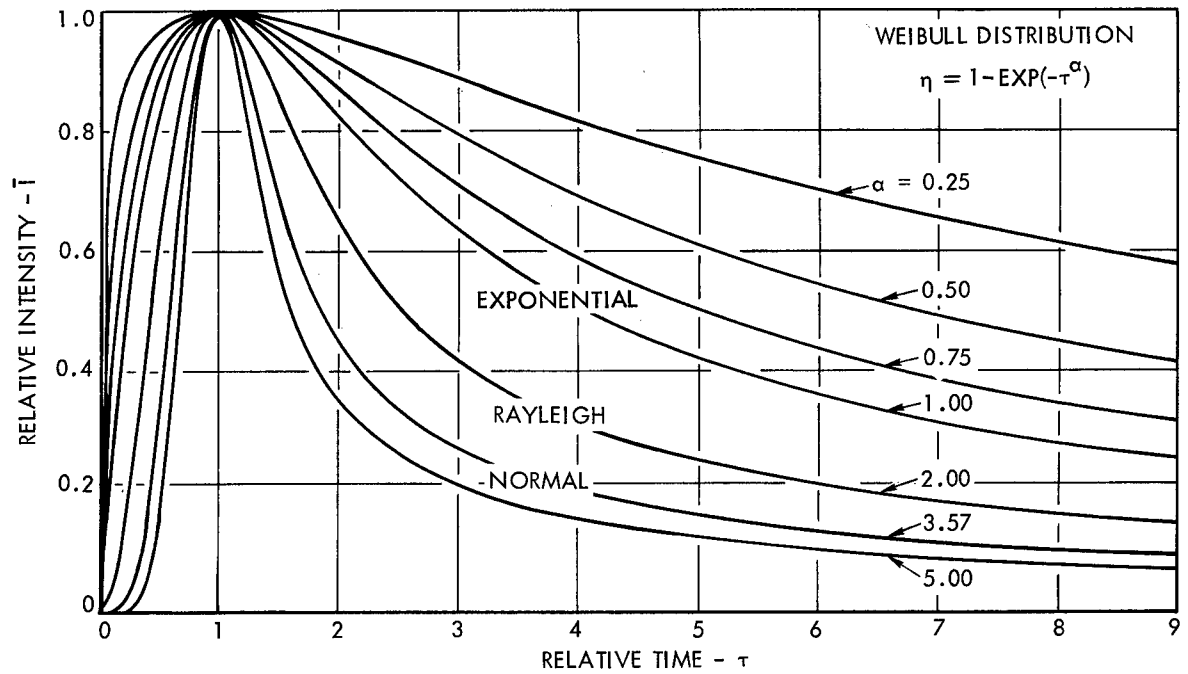


FIGURE 32 - THEORETICAL PREDICTION OF THE EFFECT OF TIME ON INTENSITY OF EROSION WHEN $n = 4$

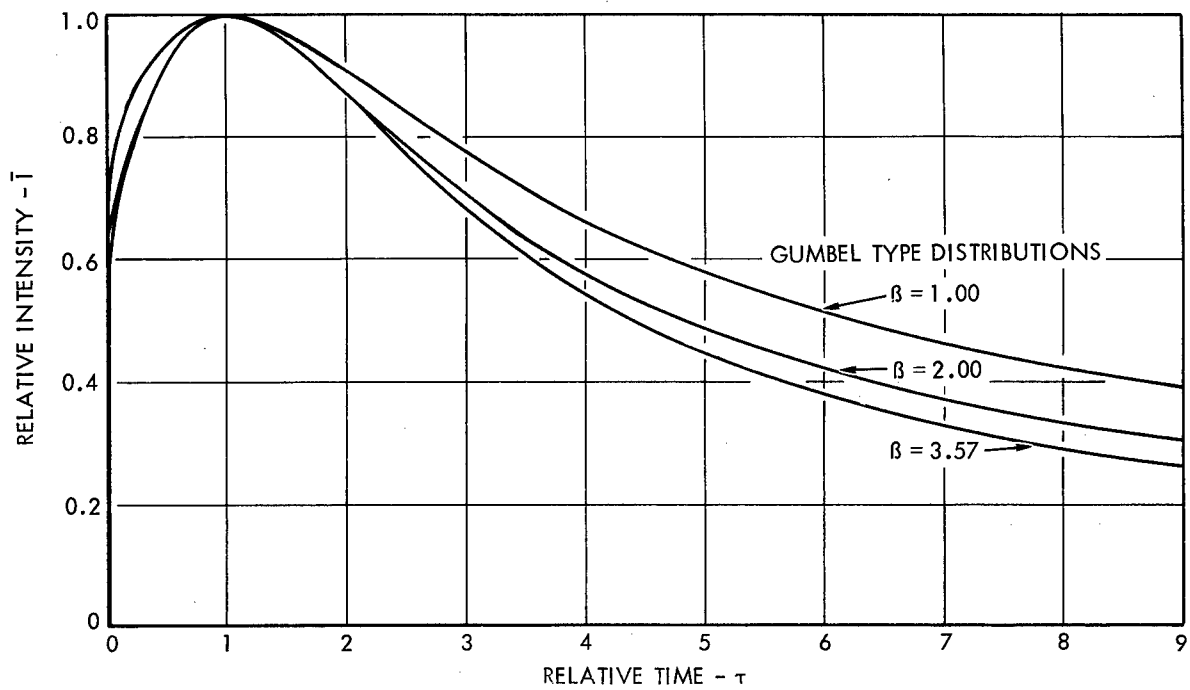


FIGURE 33 - THEORETICAL PREDICTIONS OF THE EROSION INTENSITY WHEN GUMBEL TYPE DISTRIBUTIONS ARE USED

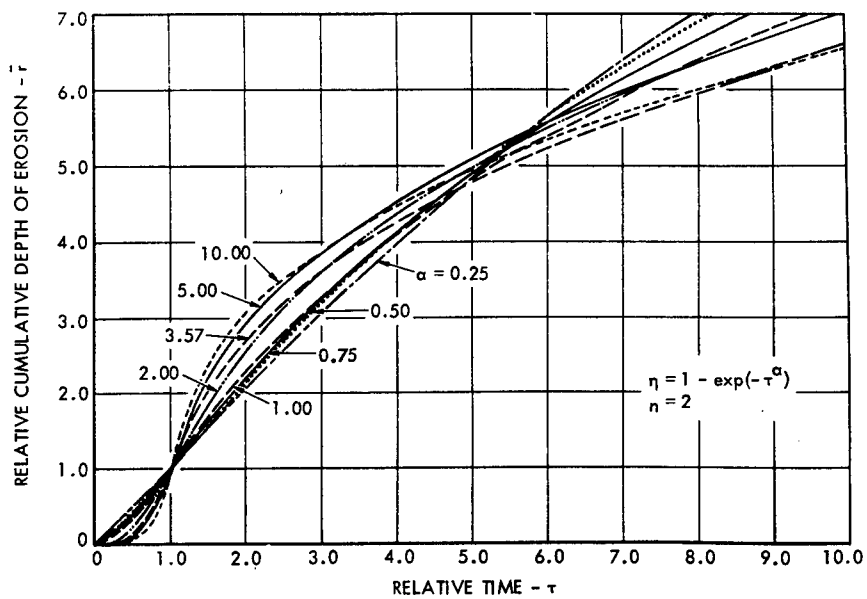


FIGURE 34 - THEORETICAL PREDICTIONS OF THE CUMULATIVE DEPTH OF EROSION